Numerical Conjugate Heat Transfer Analysis of a Roots Blower

Matuzović, Mario

Master's thesis / Diplomski rad

2022

UNIVERSITY OF ZAGREB
FACULTY OF MECHANICAL ENGINEERING AND NAVAL ARCHITECTURE

MASTER'S THESIS

Mario Matuzović

Zagreb, 2022.

UNIVERSITY OF ZAGREB
FACULTY OF MECHANICAL ENGINEERING AND NAVAL ARCHITECTURE

Numerical Conjugate Heat Transfer Analysis of a Roots Blower

Supervisors:

Prof. Željko Tuković, PhD
Prof. Ahmed Kovačević, PhD

Student:

Mario Matuzović

Zagreb, 2022.

I hereby declare that this Master's thesis is entirely the result of my own work except where otherwise indicated. I have fully cited all used sources, and I have only used the ones given in the list of references.

I would like to thank my supervisor, Prof. Željko Tuković for his excellent supervision and academic guidance. Whenever I was stuck or unsure about my approach, he would always find time for discussion and could always give me good suggestions to move forward. He is the best supervisor I could have asked for.

I would like to thank my second supervisor, Prof. Ahmed Kovačević, for giving me the opportunity to write this thesis in collaboration with City, University of London and for providing valuable guidance and support I needed throughout this project.

In addition to thanking my supervisors, I would also like to express my appreciation to Dr Sham Rane for his invaluable insights, help in overcoming problems in my research, and for always being ready to answer all my questions.

I would also like to acknowledge the Royal Academy of Engineering and Howden Compressors for providing the opportunity to cast my research in the field of compression as a part of their collaborative project SECRET with City, University of London.

Finally and most importantly, I would like to thank my parents, to whom I dedicate this thesis. Couldn’t have done it without your unconditional love and support. And of course, to my girlfriend, thank you for unwavering support and patience throughout my studies.

Mario Matuzović

SVEUČILIŠTE U ZAGREBU
FAKULTET STROJARSTVA I BRODOGRADNJE
Središnje povjerenstvo za završne i diplomske ispite
Povjerenstvo za diplomske ispite studija strojarstva za smjerove:
Procesno-energetski, konstrukcijski, inženjersko modeliranje i računalne simulacije i brodostrojarski

Sveučilište u Zagrebu Fakultet strojarstva i brodogradnje	
Datum	Prilog
Klasa: **602 - 04 / 22 - 6 / 1**	
Ur.broj: **15 - 1703 - 22 -**	

DIPLOMSKI ZADATAK

Student: **Mario Matuzović** JMBAG: 0035188291

Naslov rada na hrvatskom jeziku: **Numerička analiza spregnutog prijelaza topline u Roots-ovom puhalu**

Naslov rada na engleskom jeziku: **Numerical Conjugate Heat Transfer Analysis of a Roots Blower**

Opis zadatka:

A Roots blower which will be investigated operates without the need for internal lubrication and is used for low pressure ratio applications. The rotors are separated by a precisely engineered gap through which air can escape causing losses. The prediction of temperature distribution and thermal expansion due to thermal loads is critical in the design of rotor-to-rotor and rotor-to-casing clearance gaps. The aim of this study is to numerically analyse the heat transfer from the pressurized air to the rotors and casing and provide the temperature distribution over the structural elements. This will help in understanding the physics behind leakage flow phenomena and ensure safe operation of rotary positive displacement machines.

Numerical model will be developed and solved using optimized and commercially available ANSYS CFD code. The dynamic grids will be generated by the commercial software SCORG and imported into ANSYS. The physical setup will be interrogated directly by using infrared thermography for temperature measurements in order to validate the results. The following tasks will be performed:

1. Perform a literature survey and describe the applied models and methods;
2. Construct a 3D finite volume mesh of the solid domain including housing, lobes and shafts for the conjugate heat transfer (CHT) model;
3. Construct a 3D dynamic finite volume mesh of the deformable fluid flow domain using the grid generation software SCORG and a 3D static mesh of the fluid domain for inlet and outlet;
4. Perform non-conjugate CFD analysis to calibrate the gap size to match test data of the flow;
5. Perform CHT analysis and produce results for measured operating conditions. Calculations will be performed with the uniform gap size adjusted to match the measured flow;
6. Analyse the results of the simulations and compare with experimental data.

It is advised to list references used in this work, as well as to acknowledge help and support possibly received during the course of this study.

Zadatak zadan:	Datum predaje rada:	Predviđeni datumi obrane:
3. ožujka 2022.	5. svibnja 2022.	9. - 13. svibnja 2022.

Zadatak zadao:

Prof.dr.sc. Željko Tuković Tuković Ž.

Prof.dr.sc. Ahmed Kovačević
CITY, UNIVERSITY OF LONDON

Predsjednik Povjerenstva:

Prof. dr. sc. Tanja Jurčević Lulić

TABLE OF CONTENTS

LIST OF FIGURES

LIST OF TABLES

NOMENCLATURE

Latin	Unit	Description
a	m^2/s	Thermal diffusivity
A	m^2	Surface area
c_p	$J/(kgK)$	Heat capacity at constant pressure
c_v	$J/(kgK)$	Heat capacity at constant volume
F	N	Force
k	m^2/s^2	Turbulent kinetic energy
p	bar	Pressure
q	W/m^2	Heat flux
Q	W	Heat
M	kg/mol	Molar mass
u	m/s	Velocity
V	m^3	Volume
R	J/(kgK)	Gas constant
T	K	Temperature
t	s	Time

Greek	Unit	Description
α	$W/(m^2K)$	Heat transfer coefficient
ε	m^2/s^3	Dissipation of turbulent kinetic energy
μ	$Pa \cdot s$	Dynamic viscosity
μ_T	$Pa \cdot s$	Turbulent viscosity
μ_v	$Pa \cdot s$	Volume viscosity
λ	$W/(mK)$	Thermal conductivity
ρ	$\mathrm{kg/m^2}$	Density
τ	N/m^2	Tangential stress
ω	m^2/s^2	Specific turbulence dissipation
ϕ_v	W/m^2	Volumetric heat source

Abbreviations

2D	Two-Dimensional
3D	Three-Dimensional
CA	Crank Angle
CAES	Compressed Air Storage
CFD	Computational Fluid Dynamics
CFL	Courant–Friedrichs–Lewy condition
CHT	Conjugate Heat Transfer
DNS	Direct Numerical Simulation
EU	European Union
EU27	European Union Countries from 2020

FEA	Finite Element Analysis
FEM	Finite Element Method
FSI	Fluid Structure Interaction
FVM	Finite Volume Method
IDE	Integrated Development Environment
LES	Large Eddy Simulation
PDE	Partial Differential Equations
PR	Pressure Ratio
RANS	Reynolds Averaged Navier-Stokes
RPM	Rounds per minute
SST	Shear Stress Transport
TSF	Time Scale Factor
TUI	Text User Interface
UDF	User Defined Functions
UDND	User Defined Nodal Displacement
UDNM	User Defined Node Memory
URF	Under Relaxation Factor
USA	United States of America

ABSTRACT

This thesis deals with Conjugate Heat Transfer analysis of an oil-free Roots blower which is a Positive Displacement Machine used for low pressure ratio applications. Prediction of temperature distribution is critical in the design of rotor-to-rotor and rotor-to-casing clearance gaps inside these compressors. The aim of the study is to numerically analyse the heat transfer from pressurized air to rotors and casing and provide the temperature distribution over structural elements. These problems are too complex to be solved analytically so this thesis will employ High Performance Computing to perform CFD simulations and find an approximate numerical solution of the heat transfer problem. Internal flow inside the blower is highly transient and to predict its characteristic we need to tackle one of the most challenging deforming mesh problems where working medium is displaced during simulation. To allow for mesh deformation, due to intermeshing of the rotors, the moving mesh technique will be employed in this thesis. A numerical framework for 3D simulation of complex flow field inside a Roots blower compressor is established and presented. The framework employs Finite Volume Method. Five cases are investigated, each for different operating condition. In order to evaluate the accuracy of the developed numerical model, extensive validation is performed for several operating conditions. The numerical solution is compared to the overall performance of an equivalent experimentally measured compressor. The experimental data were provided by City University London and they include measurements of surface and air temperature, mass flow rate, pressure ratio, and effective power measurements. The comparison between numerical results has shown good agreement with the experimental data. The outcome of this research contribute to the understanding of the effects of leakage flow phenomena and can help design more efficient compressors.

Keywords: Conjugate Heat Transfer, Roots blower, Positive Displacement Machine, Numerical analysis, High Performance Computing, Computational Fluid Dynamics, Moving mesh, Finite Volume Method, Leakage flow

SAŽETAK
(ABSTRACT IN CROATIAN)

Ovaj diplomski rad bavi se analizom spregnutog prijelaza topline Roots-ovog puhala koji radi bez podmazivanja te se primjenjuje za niske kompresijske omjere. Procjena temperaturne raspodjele ključna je pri projektiranju zazora koji se nalaze u kućištu ovih kompresora. Cilj rada je numerički analizirati prijenos topline s komprimiranog zraka na rotore i kućište te dati temperaturnu raspodjelu na površinama rotora i kućišta. U radu će se koristiti računalni klasteri s visokom učinkovitošču za izvođenje CFD simulacija i pronalaženje približnog numeričkog rješenja problema prijenosa topline. Predstavljena je numerička metoda za simulaciju kompleksnog strujanja radnog medija unutar Roots-ovog puhala. Metoda koristi numeričku metodu kontrolnih volumena. Provedeno je 5 simulacija, svaka za jedan ispitni uvjet. Kako bi se procjenila točnost numeričkog modela, u radu je provedena opsežna validacija za nekoliko ispitnih uvjeta. Numeričko rješenje uspoređeno je s eksperimentalnim rezultatima ekvivalentnih ispitnih točki mjerenog kompresora. Eksperimentalne podatke je dao na raspolaganje fakultet City, Sveučilišta u Londonu. Podaci uključuju mjerenja temperature površine i zraka, masenog protoka, kompresijskog omjera te mjerenja efektivne snage. Usporedba je pokazala dobro slaganje numeričkog rješenja s eksperimentalnim podacima. Ishod ovog istraživanja doprinosi razumijevanju gubitaka u volumetrijskim kompresorima te može doprinijeti povećanju njihove efikasnosti.

Ključne riječi: Spregnuti prijelaz topline, Roots-ovo puhalo, Numerička analiza, Računalni klasteri, Računalna dinamika fluida, Metoda kontrolnih volumena

PROŠIRENI SAŽETAK
(EXTENDED ABSTRACT IN CROATIAN)

UVOD

U ovom radu provedena je numerička simulacija spregnutog prijenosa topline kroz Roots-ovo puhalo. Puhalo radi bez podmazivanja zbog čega mora postojati zazor između rotora i rotora te između rotora i kućišta. Zazori su veliki izvor gubitaka te je poželjno da su što manji. Cilj rada je numerički izračunati temperaturno polje na površinama rotora i kućišta te rezultate usporediti sa eksperimentalnim mjerenjima. Za numeričko rješavanje u radu će se koristiti komercijalni CFD kod ANSYS Fluent koji koristi metodu kontrolnih volumena. Rezultati CHT analize mogu se koristiti kao rubni uvjet za strukturalne simulacije koje koriste metodu konačnih elemenata. Na taj način mogu se predvidjeti deformacije uslijed temperaturnih naprezanja u svrhu minimizacije samog zazora.

Simulacije strujanja provedene su za pet različitih ispitnih uvjeta pri čemu je za svaku ispitnu točku potrebno mijenjati veličinu aksijalnog zazora. Na taj način kompenzira se promjena masenog protoka uslijed toplinskih deformacija rotora i kućišta. CHT model pretpostavlja rotor i kućište kao kruta tijela zbog čega je potrebno kompenzirati promjene u strujanju uslijed toplinskih deformacija. Ovaj postupak opisan je u nastavku kao kalibracija zazora. Nakon kalibracije slijedi numerička analiza spregnutog prijenosa topline. Postojeći CFD model proširen je sa uključenjem prijenosa topline između krutine i fluida. Fluid koji se koristi kao radni medij je zrak.

U nastavku je opisan numerički model i diskretizacija te su prikazane konture tlaka, temperature i brzine na bitnim presjecima. Numerički rezultati su uspoređeni sa eksperimentalnim mjerenjima koje je dalo na raspolaganje Sveučilište u Londonu.

NUMERIČKI MODEL

Matematički model sastoji se od 7 diferencijalnih jednadžbi i 7 nepoznatih polja (u,v,w,p,T,k,ω). Imamo 4 skalarne jednadžbe i 1 vektorsku jednadžbu koje opisuju stlačivo, turbulentno, trodimenzijsko strujanje primjenjujući osnovne zakone mehanike fluida na infinitezimalnu česticu fluida. Naravno, potrebno je postaviti rubne uvjete da bi jednoznačno definirali diferencijalne jednadžbe. Utjecaj gravitacije je zanemaren u analizi kao i prijenos topline zračenjem. Energetsku jednadžbu je potrebno riješavati u oba slučaja, i u ne-spregnutoj CFD simulaciji, i u CHT simulaciji kroz kučište jer se radi o stlačivom mediju.

Kod modeliranja turbulencije primjenjen je k-ω SST model turbulencije koji je kombinacija k-ε i k-ω modela. Bazira se na pretpostavci da je smično naprezanje proporcionalno kinetičkoj energiji turbulencije. SST model se blizu stijenke ponaša kao k-ω što omogućava rješavanje graničnog sloja umjesto modeliranja zidnom funkcijom dok se podalje od stijenke ponaša kao k-ε model koji je jako efikasan i nije osjetljiv na rubne uvjete turbulencije. Model je tranzijentan budući da se domena rotora neprestano deformira. Priroda strujanja u Roots-ovom kompresoru je izrazito nestacionarna budući da se radi o stroju sa diskontinuiranim radom. Sve fizikalne veličine, osobito na izlazu, značajno variraju u vremenu.

Budući da su parcijalne diferencijalne jednadžbe nelinearne i mogu se riješiti samo za mali broj specijalnih slučajeva analitički, u ovom radu će biti riješene približno, numeričkom metodom kontrolnih volumena, pri čemu će se koristiti nespregnuti rješavač koji primjenjuje PISO algoritam. Pri rješavanju koriste se diskretizirani integralni oblici prethodno navedenih jednadžbi. Da bi riješili takav sustav diferencijalnih jednadžbi moramo podijeliti domenu na konačan broj kontrolnih volumena ili ćelija i na taj način, diskretizacijom vremena i prostora, pojednostavljujemo problem na određivanje vrijednosti nepoznanica u centrima kontrolnih volumena. Svaka integralna algebarska jednadžba će povezati vrijednost u središtu kontrolnog volumena, koja se nalaze u težištu volumena, sa vrijednostima u središtima susjednih ćelija. Na svaku ćeliju postavlja se integralna jednadžba te se volumni integrali pretvaraju u površinske. Interpolacijom vrijednosti u središtima susjednih ćelija dobiju se vrijednosti na kontrolnim površinama ćelije. Za ćelije koje se nalaze na granicama ekstrapoliraju se vrijednosti rubnih uvjeta. Ovim postupkom diskretizacije uvodimo diskretizacijsku grešku u rješenje i nju možemo smanjiti profinjenjem mreže tj. povećavanjem broja kontrolnih volumena u mreži ili povećavanjem reda interpolacije. Gradijenti su diskretizirani metodom najmanjih kvadrata dok su konvekcijskih članovi transportnih jednadžbi diskretizirani uzvodnom shemom drugog reda točnosti. Budući da jednadžba očuvanja količine gibanja ima nelinearni član moramo ga linearizirati oko pretpostavljenih vrijednosti i onda iterativnim postupkom mijenjamo pretpostavljene vrijednosti sve dok riješenje ne iskonvergira. Linearizacijom sustava algebarskih jednadžbi uvodimo linearizacijsku grešku u rješenje.

KALIBRACIJA AKSIJALNOG ZAZORA

Mreža je generirana na temelju zadane geometrije. Dinamička mreža napravljena je pomoću programa SCORG. SCORG je automatski generator koji generira mrežu za svaki vremenski korak potreban u simulaciji. Napravljene su dvije mreže. Jedna mreža je konformna na granici između domena dva rotora, a jedna ima ne-konformno sučelje između domena. Konformna mreža je inače točnija jer se na taj način izbjegavaju interpolacije sa težinskim vrijednostima površina na granicama između dvije domene. Međutim, SCORG specifično za geometriju Roots-ovog puhala generira kvalitetniju ne-konformnu mrežu.

Računalna domena prikazana je na slici ispod. Podjeljena je na pet dijelova:

- Inlet (plavo)
- Inport (tirkizno)
- Rotor domain (žuto)
- Outport (narančasto)
- Outlet (crveno)
- Axial clearance (ljubičasto)

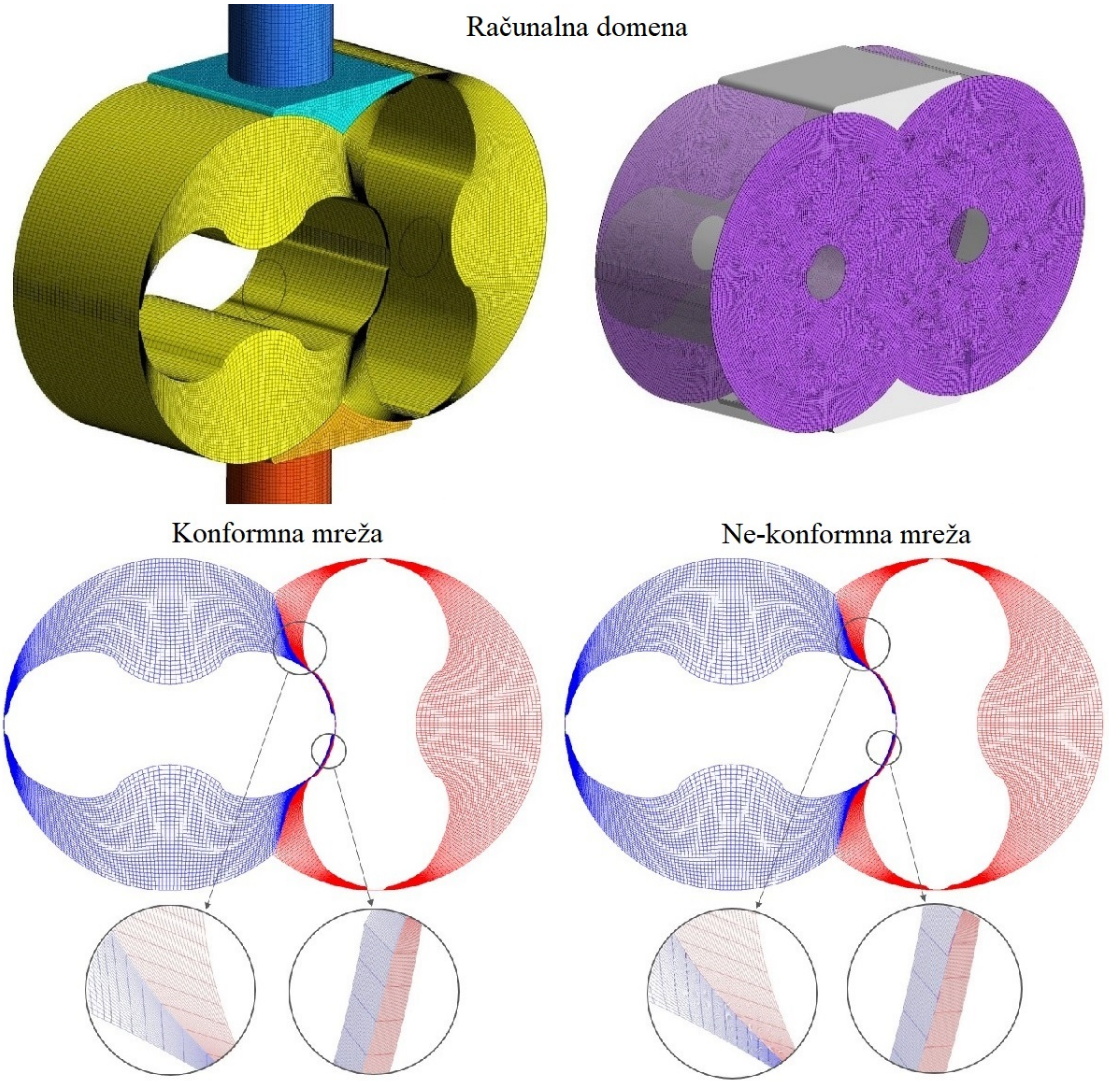

Slika 1 Računalna domena ne-spregnutog CFD modela

Dinamička mreža se ostvaruje preko *User Defined Functions* u Fluentu. Korištena je *smoothening* opcija zajedno sa *in-cylinder* specifikacijom. Sve mreže su spojene u jednu preko nekonformnih sučelja. Kompozitna mreža kontrolnih volumena sastoji se od oko 1 366 176 kontrolnih volumena. Budući da imamo 7 nepoznanica dobit ćemo sustav od približno 95 milijuna algebarskih jednadžbi. U dinamičkoj domeni ima oko 573 500 čvorova čija je translacija kontrolirana preko UDF-ova. Zbog velikih problema sa stabilnošću simulacije pristup sa primjenom ne-konformne mreže je odbačen. Naime, uslijed stvaranja ne-konformnog sučelja između dvije dinamičke zone Fluent generira unutrašnju zonu da bi povezao ćelije koje nisu usklađene i pri tome generira mnoštvo neispravnih ćelija zbog čega dolazi do divergencije.

Za svaku ispitnu točku odrađeno je 2160 vremenskih koraka. Broj iteracija po vremenskom koraku iznosi 50, sve dok reziduali nisu pali na prihvatljivu razinu od 10e-3. Osim reziduala praćeni su momenti na muškom i ženskom rotoru, protok zraka kroz kompresor te izlazna temperatura zraka. Različite vrijednosti protoka ostvareni su mijenjanjem statičkog tlaka na izlazu iz domene. Statički tlak i temperatura na ulazu su približno isti za sve ispitne točke. Tablica 1 prikazuje fizikalne veličine izmjerene eksperimentalno. Sukladno toj tablici definirani su navedeni rubni uvjeti u simulaciji.

Tablica 1 Eksperimentalni podaci za pojedine ispitne točke

Tlak na ulazu [bar]	Temperatura na ulazu [°C]	Tlak na izlazu [bar]	Temperatura na izlazu [°C]	Protok [kg/s]
1.024	29.66	1.24	52.46	0.0033
1.024	29.19	1.232	59.06	0.0063
1.023	30.03	1.23	57.72	0.0092
1.023	30.92	1.439	82.31	0.0078
1.023	33.8	1.635	139.05	0.007

U nastavku su dani rezultati za pet provedenih simulacija. Cilj ne-spregnute CFD simulacije bio je kalibrirati zazor i ostvariti validaciju snage i protoka. Sva 3 cilja su uspješno ostvarena te su rezultati prikazani u tablici ispod. Tablica 2 prikazuje veličinu kalibriranog aksijalnog zazora te izračunati protok i snagu u ovisnosti o broju okretaja i kompresijskom omjeru. Također, prikazano je i odstupanje od eksperimentalo izmjerene snage i protoka. Odstupanje je u prihvatljivim granicama. Iz tablice 2 također je vidljivo da su numerički izračunate temperature nešto više od izmjerenih. To je očekivano budući da su zidovi definirani kao adijabatski. Zbog izostanka prijenosa topline sa zraka na rotor i kućište ostvarene su više temperature na izlazu.

Tablica 2 Numerički rezultati za pojedine ispitne točke

	Maseni protok [kg/s]	Odstupanje protoka %	Moment [Nm]	Snaga [kW]	Odstupanje snage %	Aksijalni zazor [um]	Izlazna temp. [°C]
1000 o/min omjer 1.2	0.00305	-7.53	1.56	0.16	-1.40	185	69
1500 o/min omjer 1.2	0.00614	-2.59	1.58	0.25	2.81	224	67
2000 o/min omjer 1.2	0.00947	2.97	1.62	0.34	4.27	250	66
2000 o/min omjer 1.4	0.00778	-0.25	3.14	0.66	1.78	190	105
2000 o/min omjer 1.6	0.00665	-5.04	4.57	0.96	0.72	143	168

Slika 2 jasno prikazuje povratni tok vrućeg zraka kroz zazore i njegovo miješanje sa hladnim ulaznim zrakom. Izlazna temperatura za trenutni vremenski korak iznosi 170 °C te je ujedno i najviša postignuta temperatura u odnosu na ostale ispitne uvjete.

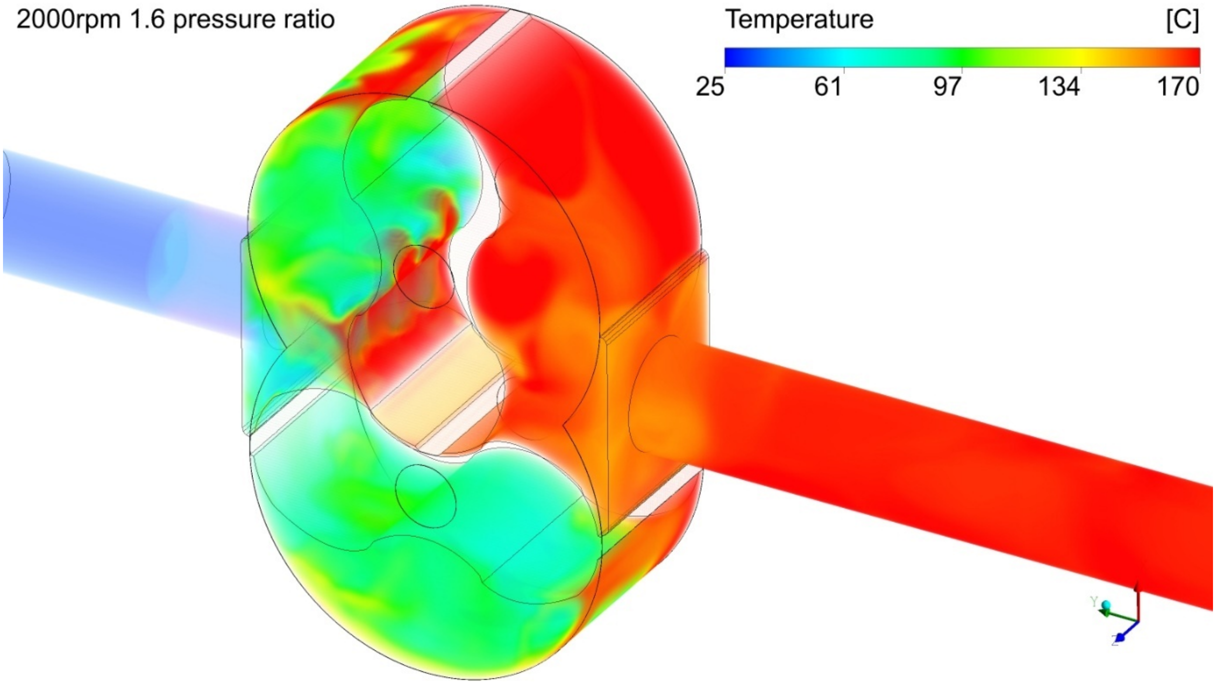

Slika 2 3D Temperaturno polje za 2000 o/min i kompresijski omjer 1.6

Na slici 3 se također vidi povratni tok zraka kroz zazore kao i utjecaj aksijalnog zazora na polje brzine. Na krajevima rotora, odmah na vrhu, dolazi do stvaranja dva vrtloga koji konvergiraju prema sredini rotora. Zrak se prolazeći kroz zazore ubrzava te upravo u zazoru postiže svoju maksimalnu brzinu. Kako su svi ciljevi u ovom poglavlju uspješno ostvareni, numerički model se proširuje sa uključenjem prijenosa topline na kućište i rotor.

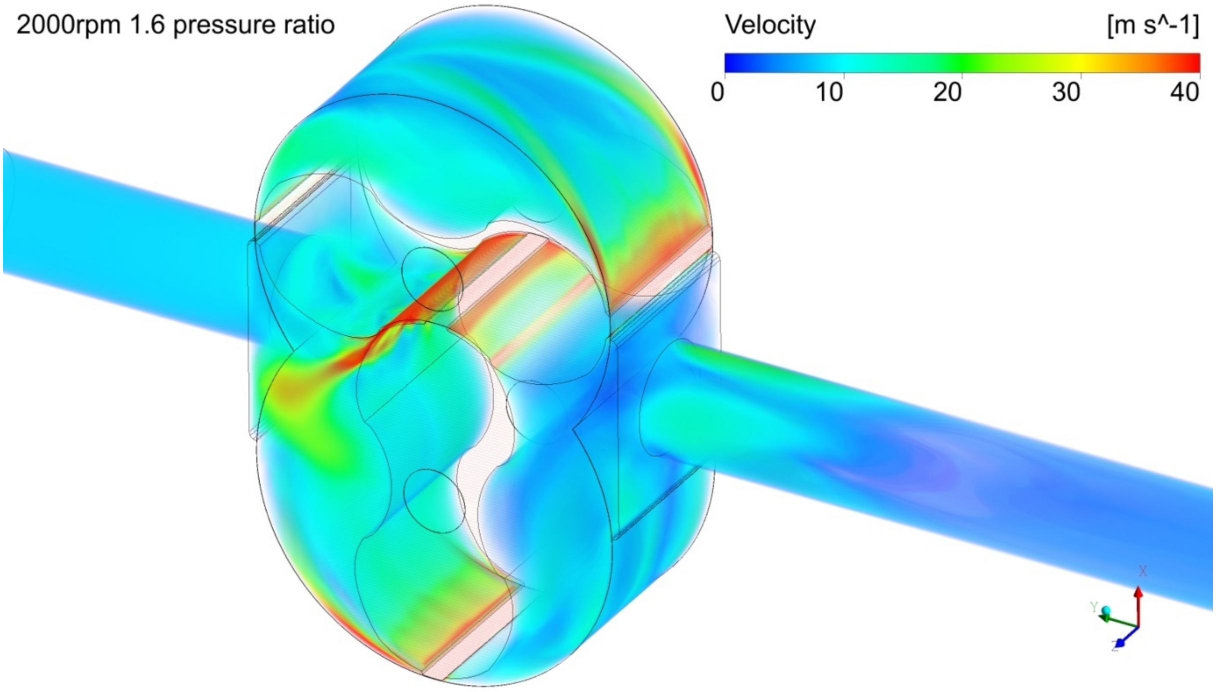

Slika 3 **3D polje brzine za 2000 o/min i kompresijski omjer 1.6**

SIMULACIJA SPREGNUTOG PRIJENOSA TOPLINE

Cilj ove simulacije bio je ostvariti validaciju temperature zraka na izlazu te temperature površine rotora i kućišta uz zadržavanje validacije snage i protoka. Postojeća geometrija za svaku ispitnu točku zajedno sa pripadajućim aksijalnim zazorom nadograđena je sa elementima kućišta, rotora, safirnog stakla te ploče za pričvrščenje. Zupčanici koji se inače nalaze unutar kućišta mjenjača nisu uključeni u analizu. Prikaz računalne domene koja prikazuje sve ove elemente te generirana sučelja nalazi se na slici 4.

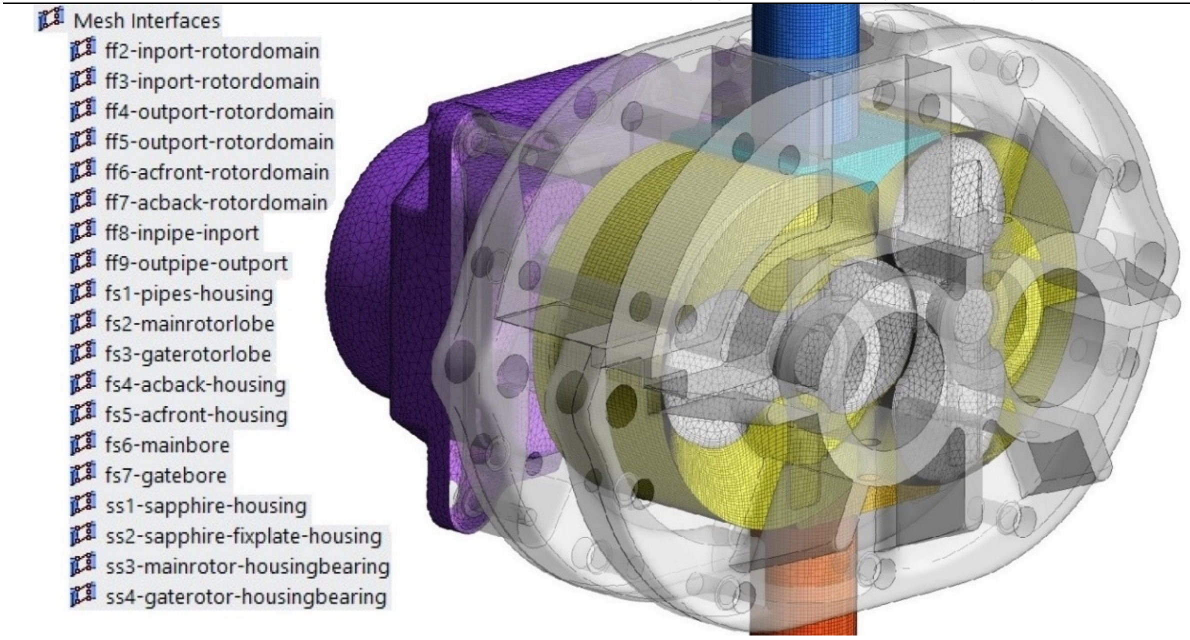

Slika 4 Računalna domena CHT modela

Model sadrži ukupno 2 648 939 ćelija i 19 ne-konformnih sučelja:

- 8 fluid-fluid sučelja
- 7 fluid-solid sučelja
- 4 solid-solid sučelja

S konvergiranim rješenjem iz prošle simulacije nastavilo se u slijedeću spregnutu simulaciju prijenosa topline za koju je odrađeno 5040 vremenskih koraka. Postavke simulacije su ostale iste. Najveća promjena jest definiranje spregnutih termalnih rubnih uvjeta na sučeljima fluid-krutina i krutina-krutina. Na vanjskim granicama definirana je konvekcija sa koeficijentom prijelaza topline 10 $\mathrm{W/(m^2K)}$ i temperaturom okoline 300 K. Proces provođenja u krutini je ubrzan radi postizanja približno stacionarnog stanja temperaturnog polja u krutini koje bi odgovaralo realnom radnom vremenu kompresora od 70 minuta.

Tablica ispod prikazuje numeričke rezultate. Model je zadržao validaciju snage i protoka te je ostvarena validacija izlazne temperature zraka. Model treba pouzdano predvidjeti izlaznu temperaturu zraka koja je u prošlim simulacijama s razlogom bila povišena u odnosu na mjerenja. Opaža se vrlo dobra korelacija između eksperimentalnih mjerenja izlazne temperature i numeričkog rješenja.

Tablica 3 Numerički rezultati CHT analize

	1000 o/min omjer 1.2	1500 o/min omjer 1.2	2000 o/min omjer 1.2	2000 o/min omjer 1.4	2000 o/min omjer 1.6
Temperatura inicijalizacije krutine [°C]	37	52	52	72	117
Akumulirani vremenski korak krutine [min]	70	70	70	70	70
Akumulirani vremenski korak fluida [s]	0.84	0.56	0.42	0.42	0.42
Izlazna temperatura zraka	51	58	57	84	143
Maseni protok [kg/s]	0,0036	0.0066	0.0098	0.0083	0.00735

Slike u nastavku prikazuju usporedbu numerički izračunatog temperaturnog polja i termograma dobivenih infracrvenom termografijom. Cilj je kvantitativno podudaranje raspona temperatura i kvalitativno podudaranje kontura temperaturnog polja. Termograme je dao na raspolaganje Sveučilite u Londonu. Termogrami na slici 5 pokazuju dobro podudaranje temperature vanjskih površina kompresora sa eksperimentalnim podacima. Slike 6 i 7 prikazuju temperaturno polje na površini rotora. Može se uočiti da su konture na sredini vrha rotora malo drugačije te se primjećuje lokalno povećanje temperature na tom mjestu. Kvantitativni raspon se jako dobro slaže sa eksperimentalni mjerenjima.

2000rpm 1.6
pressure ratio

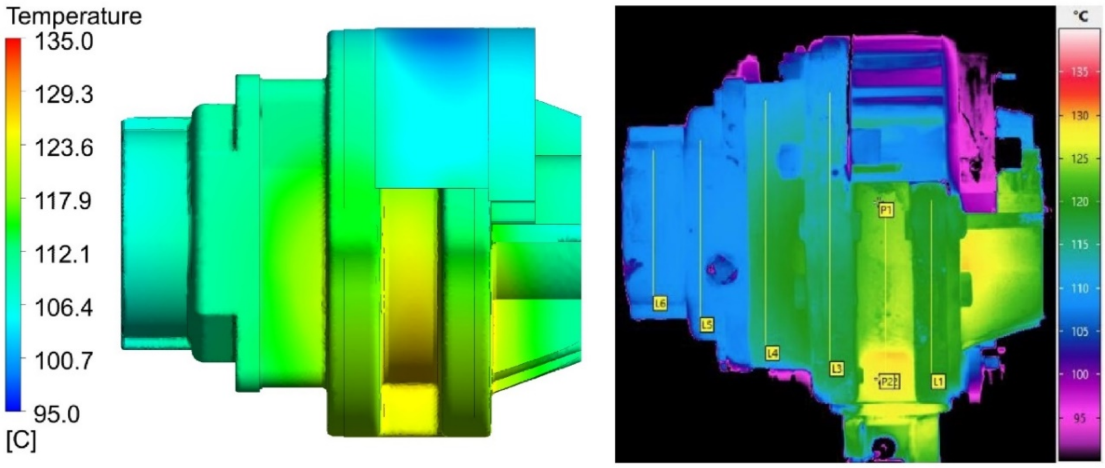

2000rpm 1.4
pressure ratio

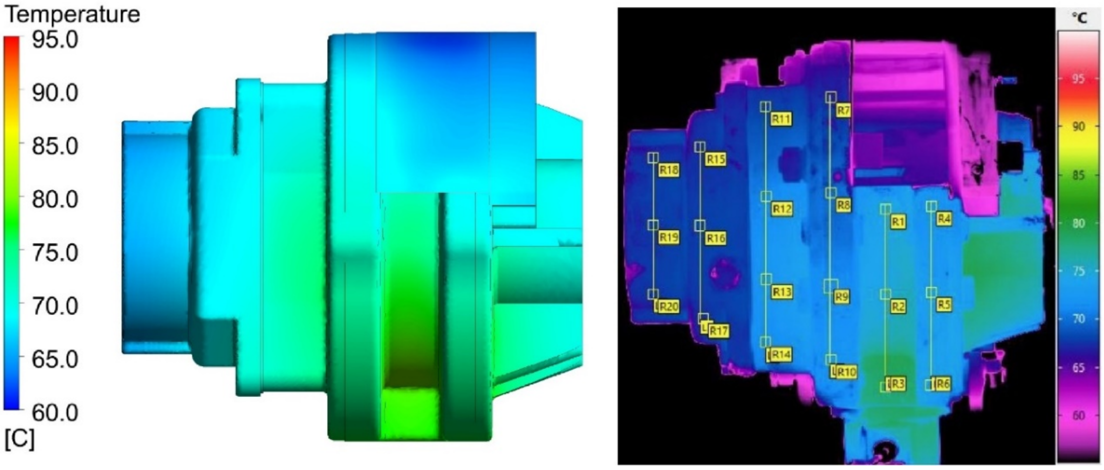

Slika 5 **Temperaturno polje na vanjskim površinama za omjer 1.6 i 1.4**

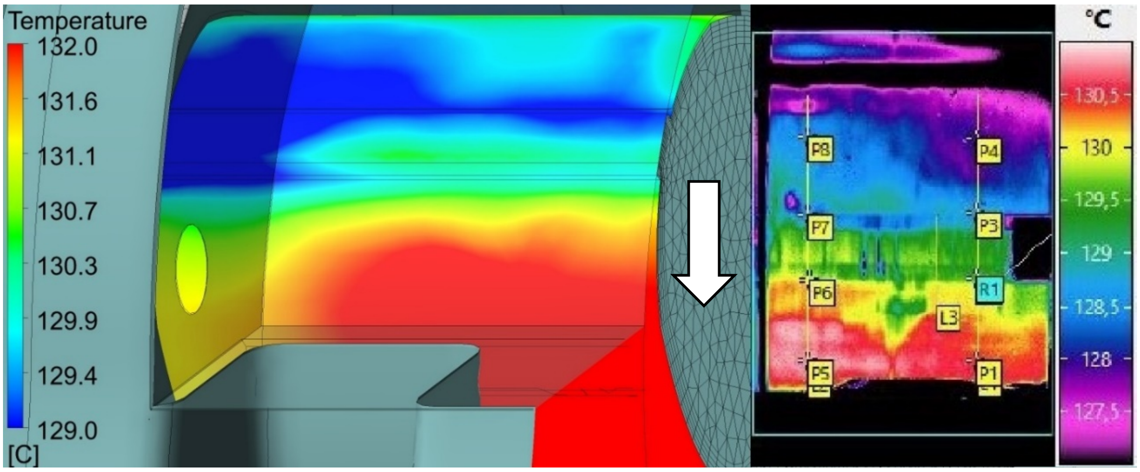

Slika 6 **Temperaturno polje na rotoru za 2000 o/min i 1.6 omjer**

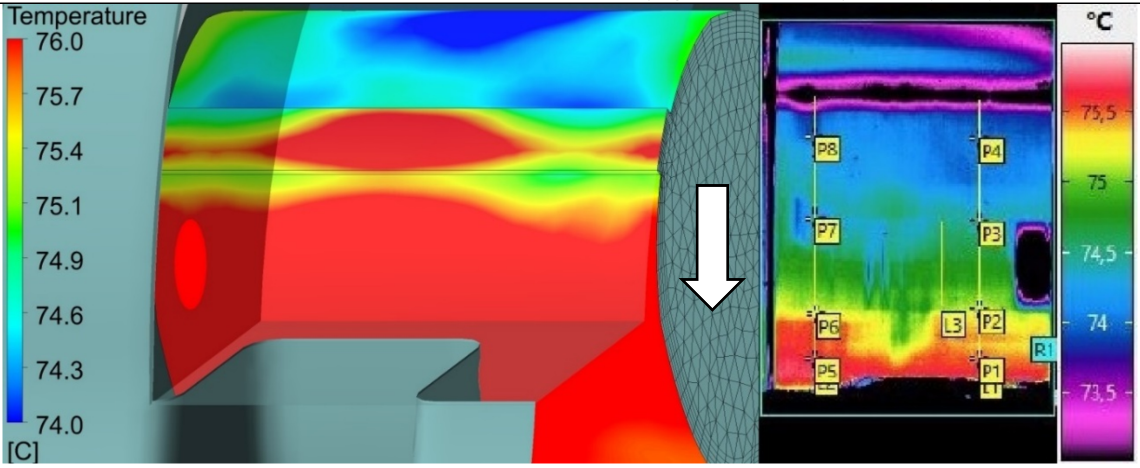

Slika 7 Temperaturno polje na rotoru za 2000 o/min i omjer 1.4

ZAKLJUČAK

U radu je provedena analiza spregnutog prijelaza topline u Roots-ovom kompresoru. Predstavljena je numerička metoda koja se temelji na metodi kontrolnih volumena. Provedeno je 5 simulacija, za po jedan ispitni uvjet. Kako bi se procjenila točnost numeričkog modela, u radu je provedena opsežna validacija. Ostvareno je jako dobro podudaranje numeričkih rezultata sa eksperimentalnim mjerenjima protoka, snage i izlazne temperature zraka. Odstupanja su u prihvatljivim granicama. Validacija temperature površine rotora i vanjskih površina ostvarena je djelomično. Iz termograma se može vidjeti jako dobro preklapanje između temperaturnih raspona na površinama rotora i na vanjskim površinama kućišta. Međutim, postoje jasno vidljiva kvalitativna odstupanja u konturama temperaturnih polja na površinama rotora. Iz svega se zaključuje da numerički model zadovoljavajuće opisuje strujanje fluida u Rootsovom kompresoru. U daljnjim razmatranjima potrebno je napraviti analizu osjetljivosti mreže te detaljnije istražiti utjecaj koeficijenta prijelaza topline na temperaturno polje u rotoru i kućištu kompresora.

1. INTRODUCTION

1.1. Background

European countries have placed special emphasis on increasing energy efficiency and reducing power consumption to counteract global warming caused by anthropogenic activities which increase concentrations of atmospheric pollutants. By minimizing energy waste we directly reduce the use of fossil fuels and pollutants in the form of greenhouse gases because fossil fuels are still the largest source of energy for electricity production. Compressed air systems account for 10% of total industrial energy use in European Union countries [1] so continued development could offer large energy savings and widen areas of their application. Chart in Figure [1] below shows that there are opportunities for improvement as operating energy cost is the greatest cost of these systems and may contribute more than 75% of the total costs during its utilization period.

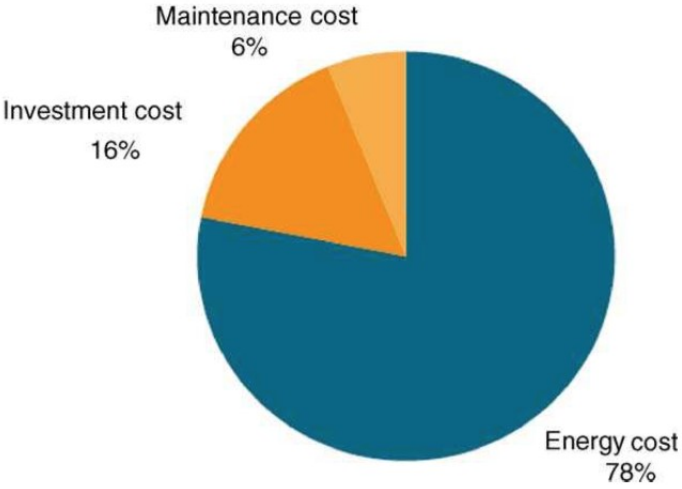

Figure 1 Life cycle costs of compressed air systems [1]

Compressors will also play an increasingly important role in future energy systems. As our energy systems increasingly rely on intermittent solar and wind technologies, grid imbalance becomes much more volatile. Compressed energy storage provides a long-term grid balancing solution. Green hydrogen storage is a cheaper alternative to batteries and have much higher energy density and low rate of self-discharge [2]. Excess electricity from the grid is used to create hydrogen through electrolysis. This hydrogen is compressed into storage tanks and can be used later in fuel cells or to power gas turbines and produce electricity in times of peak demand. Leakage reduction as a mechanism of minimizing energy losses is especially important in compressors which use hydrogen as working medium since hydrogen, due to its relatively low molecular weight, easily leaks during operation [3]. Another alternative to the hydrogen energy storage is compressed-air energy storage (CAES).

Except air and hydrogen-rich gases, compressors also process refrigerants such as freons, ammonia and propane in air conditioning and refrigeration sector, as well as carbon dioxide in the fertilizer and petroleum industries. Compressors are needed to operate pneumatic equipment which use compressed air as an energy source. They also produce active air which is used in chemical, automotive and pharmaceutical industries and comes directly into contact with products. Improving energy efficiency will reduce operating costs in all these industries, in addition to helping the environment by lowering greenhouse gas emissions. Figure 2 [4] shows that the electricity price has gradually increased over the last 14 years. Reducing utility bills makes energy more affordable and electricity prices less prone to volatility.

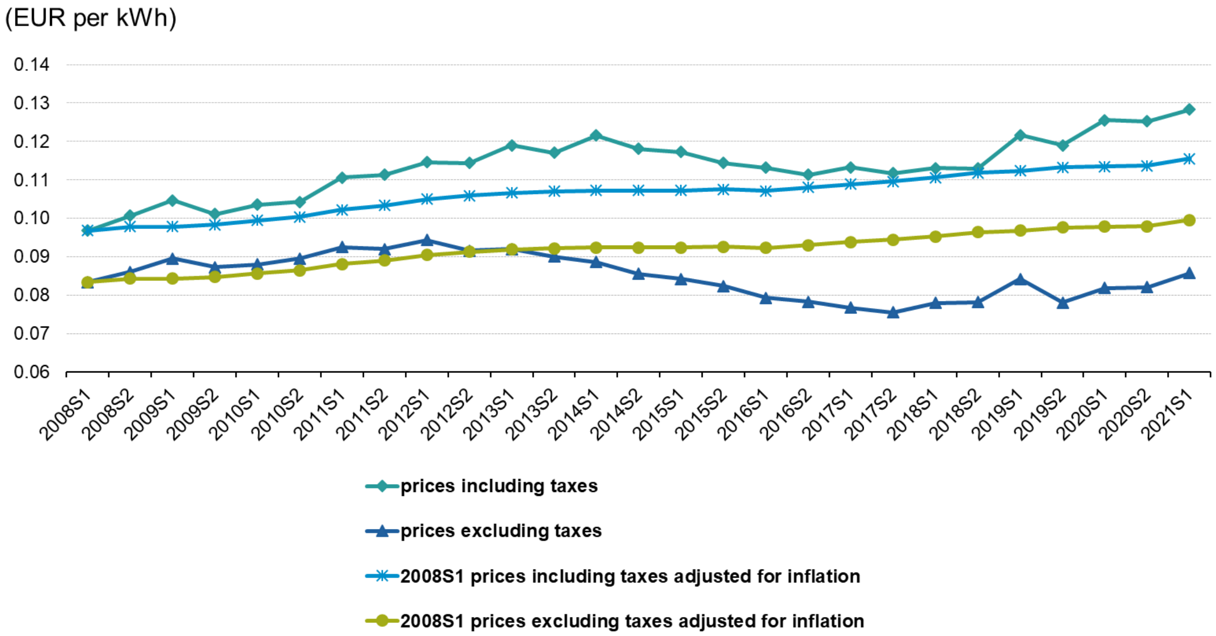

Figure 2 Development of electricity prices for non-household consumers, EU27 [4]

The thesis will explore the complex flow field inside a Roots blower compressor with CFD simulations. This will help in understanding the physics behind leakage flow phenomena which represents one of the most important loss mechanisms inside rotating machinery. The research is motivated by the principles of the European Green Deal which was proposed and adopted by European Commission and aims at achieving climate-neutrality by 2050. With its Energy Efficiency Directive EU set requirements which need to be fulfilled in order to meet energy efficiency targets. Directive was amended last time in 2018 to meet the 2030 consumption targets and savings.

The thesis will be conducted as a part of a collaborative project between Howden and City, University of London's Centre for Compressor Technology. The project Smart Efficient Compression, Reliability and Energy Targets (SECRET) aims to improve environmentally friendly oil-free machines by researching the effects of leakage flow and heat transfer inside clearance gaps. The project is supported by The Royal Academy of Engineering (RAEng) and its program greatly aligns with the objectives presented in the European Green Deal. The aimed enhancements will reduce environmental impact and reduce energy consumption by increasing efficiency and improving reliability of these machines.

1.2. Positive displacement machines

Compressors can be classified according to Figure 3 [5]. Rotary compressors are a class of compressors which operate using the positive displacement principle and transfer energy by employing rotary motion. They are categorized as a subset of positive displacement compressors which are characterized by flow intermittency. Both, reciprocating and rotary compressors, discharge gas in discrete pulses which are transmitted downstream. The main distinct features of rotary compressors are rotary motion and the absence of intake and exhaust valves, in contrast to reciprocating which employ translation and have valves. Aerodynamic compressors have continuous compression without flow interruption and are divided into centrifugal, axial and ejectors. Their energy conversion mechanism is governed by aerodynamic laws in contrast to positive displacement machines where the increase in pressure of working medium is achieved by changing the volume of working chamber.

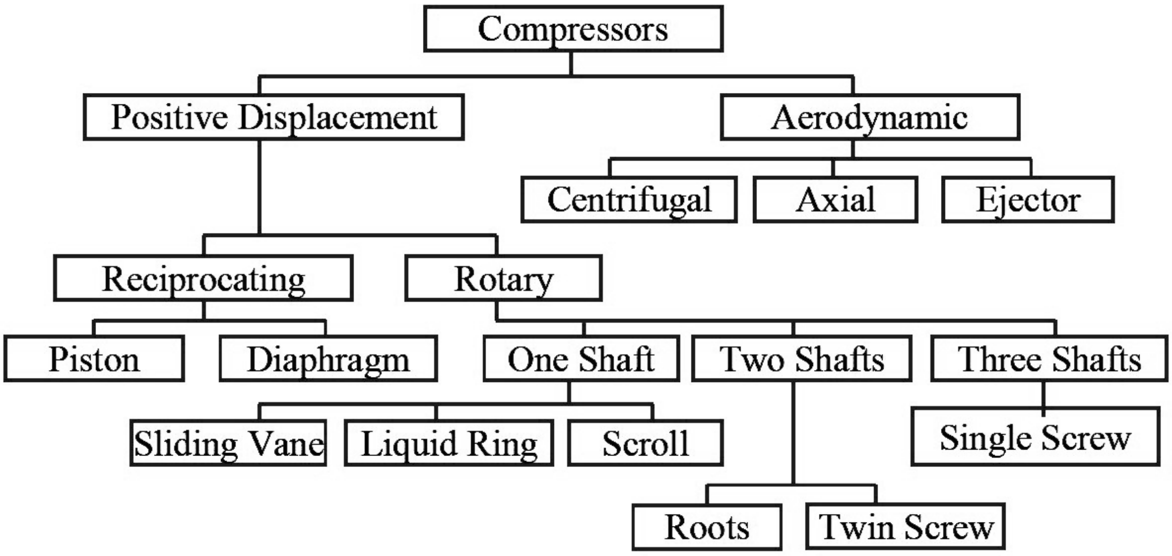

Figure 3 Common profiles of rotors in a Roots blower (adapted from reference [5])

Positive displacement machines have application in low flow rate requirements where centrifugal compressors are too uneconomical (Figure 4 [6]). They have no minimum throughput volume requirement while aerodynamic compressors can't operate below a certain minimum throughput. This makes them great in low-volume applications. Application range of rotary compressors is just in between the reciprocating and centrifugal compressors while axial compressors are used for high flow applications according to Figure 4 [6].

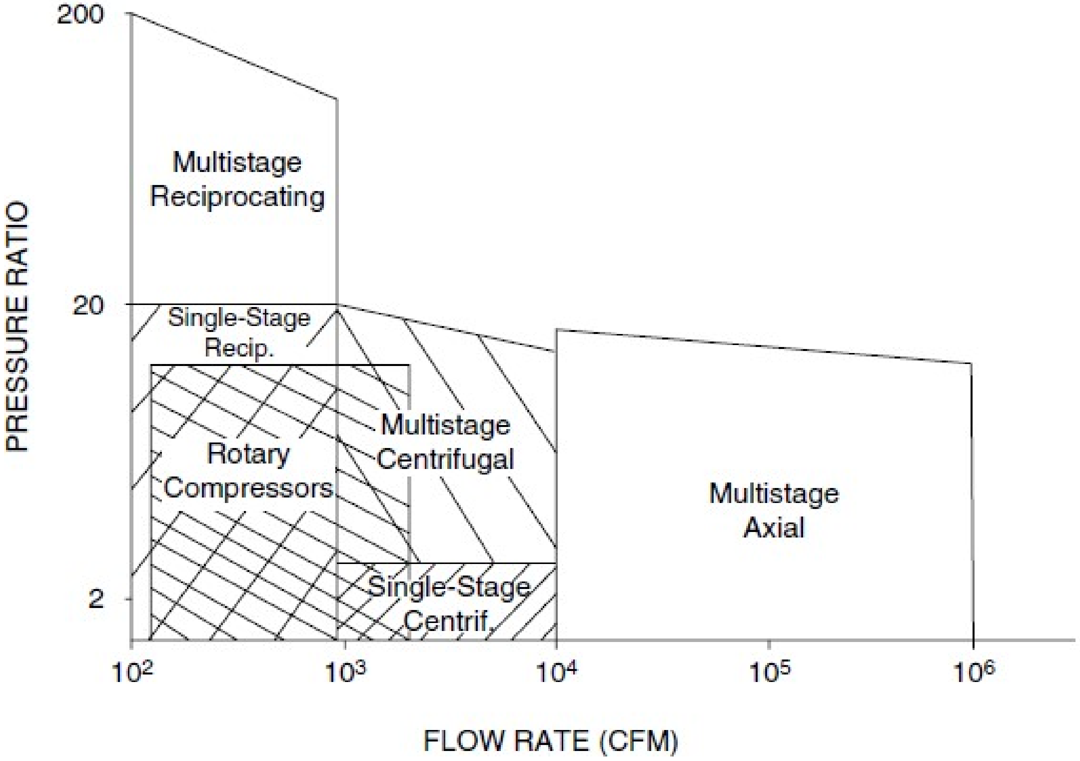

Figure 4 Application range for different types of compressors [6]

Roots and twin screw compressors are a subset of two shafts rotary compressors. Screw compressor has two intermeshing helical or spiral lobes which compress trapped air by decreasing the volume of the chamber as it moves axially along the rotor. The helical-lobe screw compressor is the most advanced rotary compressor and can achieve the highest pressure ratios in the rotary compressor group. Roots blower has straight lobes and is generally much less sophisticated.

1.3. Roots blowers

As already mentioned, Roots blowers are a variant of rotary-type positive displacement compressors which are commonly referred to as straight-lobe compressors. The first blower was developed and patented by Philander and Francis Roots, the two brothers from Indiana, USA.

A Roots blower which will be investigated operates without the need for internal lubrication and is used for low pressure ratio applications. The air delivered is oil-free and can be used in industrial processes in pharmaceutical, chemical, textile and food industry. This is especially important for processes which can't tolerate contamination because air comes directly into contact with products. This air has to be clean, contaminant free and have appropriate humidity. Oil free in this case refers to not having oil in the compression space. The compressor is not completely oil-free because the oil is still needed inside the bearings. By applying magnetic bearings, completely oil-free and environmentally friendly equipment version of this compressor can be achieved.

1.3.1. Operating principle

These types of compressors incorporate a set of identical timing gears to prevent contact between the rotors unlike oil-injected compressors where the driven main rotor interacts with the gate rotor. In oil-injected compressors oil is used as a lubricant in order to prevent direct contact and reduce wear. Without the lubricant the resulting contact would destroy this type of a compressor in which one rotor drives the other one by direct contact.

The Roots blower consists of a pair non-contacting rotors which rotate in opposite directions within a casing that encloses them. The rotors are also described as the female or gate rotor and the male or main rotor. They are separated by a precisely engineered gap through which air can escape causing losses. The gap is maintained by timing gears on each rotor which keep synchronous rotation of the rotors. Due to existence of clearance gaps pressure ranges are very limited and are frequently used as boosters placed in front of a larger compressor.

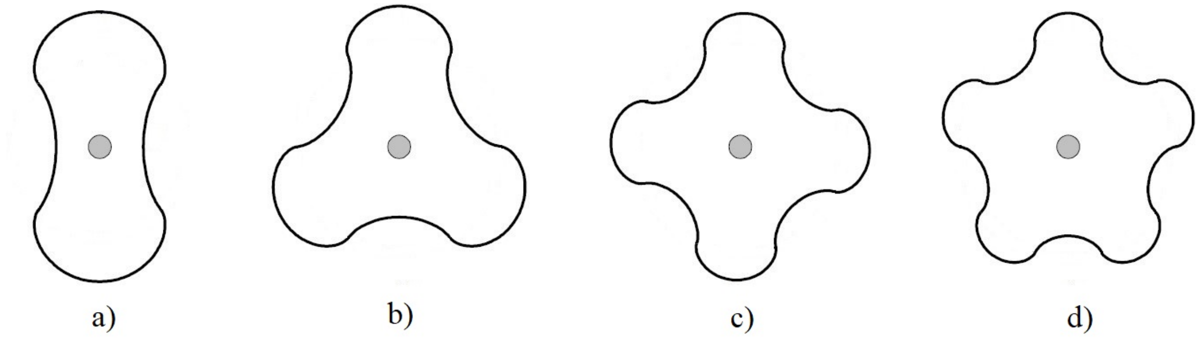

Figure 5 Common lobe configurations (adapted from reference [7])

A rotor may have different lobe profiles according to Figure 5 [7]. Two-lobe and three-lobe rotors are the most common. The three-lobe compressors have a stiffer rotor and can sustain higher pressure ratios with less difficulty [6, p. 159] than their two-lobe counterpart. Generally, more lobes mean higher efficiency.

Figure 6 [9] shows the working principle of this gas transport device. At the intake port, as the lobes rotate away from each other, air at atmospheric pressure gets drawn into the transferring chamber and sealed against the casing. In position 1 the chamber is disconnected from the intake port. As the lobes continue to rotate the volume of air is displaced from the intake to the discharge port. Because of this, pressure starts building up within the outpipe as more and more air flows into it. There is no compression of trapped air happening inside the compressor as it gets displaced by the rotary motion of the lobes since the volume of the chamber remains constant while rotating. Actual compression starts in position 2 when the lobe uncovers the discharge port and the chamber undergoes backflow or reflux of high pressure air from the port. The mixing of air increases the pressure of air trapped inside [8]. Essentially, air is allowed to flow back in order to carry out the compression. This process is repeated four times per revolution in the case of a two-lobe rotor. At the end the trapped air is pushed through the outpipe.

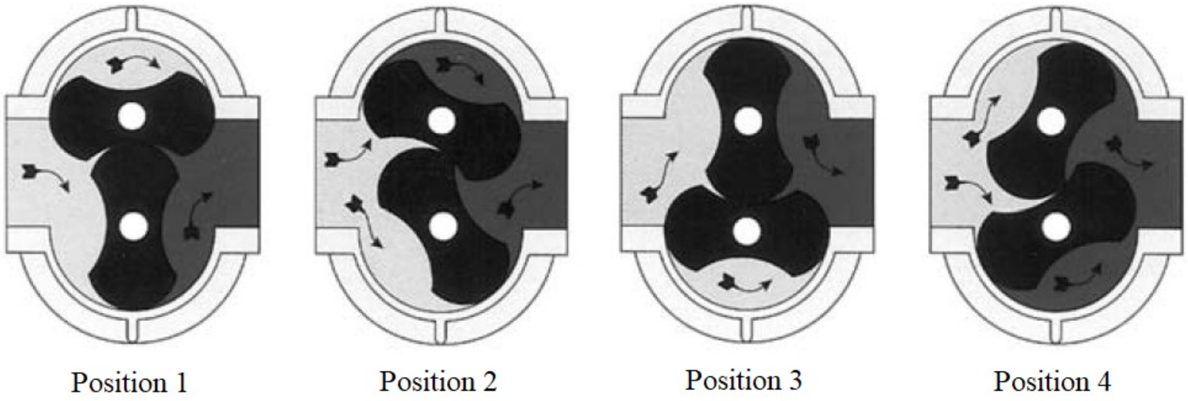

Figure 6 Roots blower operating positions [9]

1.3.2. Characteristics and performance

Due to its simple construction, small number of mechanical components and low maintenance requirements it is used in a great number of industrial processes. They can be used in applications where wide range of gas mass flow rates are needed.

As was alluded to earlier, Roots blower can achieve limited pressure ratio within a single stage due to existence clearance gaps. There are three types of gaps in the blower, namely the interlobe or rotor-to-rotor gap, the tip or rotor-to-casing gap and the axial gap through which compressed air can escape. This leakage flow from the higher pressure area to the lower pressure area leads to lower volumetric efficiency than in oil injected version of the machine. Volumetric efficiency is determined by the tip leakage past the rotors and is a function of the rotor diameter and differential pressure for a given gas. It is determined experimentally by keeping the differential pressure fixed and gradually increasing the rotational speed [6].

The backflow from discharge port to the chamber is another important factor to consider. All Roots blower implement this specific compression process which is irreversible. This limits the application of these devices due to large amount of vibrations and flow-induced noise which accompanies this unique compression process. Aerodynamic noise is related to pressure pulsations and should be avoided. Turbulent eddies are pressure disturbances and make aerodynamic noise as well, especially in centrifugal compressors. However, in the context of the positive displacement machines the main cause lies in the backflow design that almost doubles the pressure on the lobe and on its clearance gap which is accompanied by the surge of leakage and strong pressure pulsations [10]. More lobes, generally means lower vibrations and noise levels, as well as higher efficiency.

Main characteristic of Roots blowers are:

- Rotary motion
- No intake and discharge valves
- Backflow design without internal compression by volume change
- Pulsating inflow and outflow
- Constant airflow from the displacement independent of discharge pressure conditions

1.4. Computational Fluid Dynamics

Fluid flow is governed by three fundamental conservation laws; conservation of mass, momentum and energy. Mathematical formulation of these laws lead to the governing equations of fluid flow. They describe changes in physical properties in fluids and they are the fundamental basis of all CFD problems. These equations are coupled and nonlinear which means they can be solved analytically for a very small number of special cases. Assumptions were made in terms of particular problems to find analytical solutions but, as engineers, we are interested in integral values so we don’t necessarily need the analytical solution. In CFD governing equations are solved approximately; values of pressure and velocity are calculated at certain points in the domain and added up. CFD employs numerical methods and algorithms to solve mathematical models which describe fluid flow. It converts the governing equations to a large set of algebraic equations. Due to advances in computer technology, numerical algorithms, and data structures, the code which integrates numerical models can solve the largest and most complex problems. The biggest advantage of CFD is the ability to produce accurate solution for realistic geometries and complex physics really fast. This accelerates the product development process and reduces costs. Empirical analysis by conducting physical tests on prototypes using apparatus such as wind tunnels is expensive and takes much more time. CFD can simulate conditions which can't be achieved experimentally. Often CFD analysis is performed in conjunction with experimental research to fully validate the numerical results. CFD has been increasingly more popular tool to explore positive displacement machines. This allowed engineers to analyse the dynamics and thermal flow fields of positive displacement machines and improve their design. There are few different numerical methods in CFD simulations: finite volume method, finite element method and finite difference method. The numerical technique which will be used in this research is the finite volume method. ANSYS Fluent is a commercial CFD code which implements this method.

1.5. Motivation

The prediction of temperature distribution and thermal expansion due to thermal loads is critical in the design of rotor-to-rotor and rotor-to-casing clearance gaps. In the compressor that will be investigated, temperature loads are much more significant than pressure loads since rotary lobes need to maintain a gap which limits its application to lower compression ratios.

The aim of this study is to numerically analyse heat transfer from pressurized air to rotors and casing and provide temperature distribution over the structural elements. This will help in understanding the physics behind leakage flow phenomena, an area that's not sufficiently understood in the industry. At the same time it will ensure safe operation of rotary positive displacement machines and widen the areas of their application.

Because of the complex physics behind these leakage flows it is very hard to calculate the heat transfer coefficient using simplified empirical formulae. With Conjugate Heat Transfer (CHT) analysis we can accurately predict heat transfer in solids and fluids and calculate thermal boundary conditions like the heat transfer coefficient. Heat transfer coefficients over surfaces are calculated directly within the model itself and can be transferred to a structural finite element solver which contains the physical model for determining structural stresses and deformations in the rotor. Essentially, we can replace the simple convection boundary condition with direct calculations of heat transfer coefficients from CHT simulations and transfer solid temperature fields or surface loads induced by the flow to the FEA code. This approach is called fluid Structure Interaction (FSI) simulation and allows us to perform multi-physics analysis with the aim of reducing the rotor-to-rotor and rotor-to-casing gaps. Defining the correct boundary condition is vital for the accuracy of thermal analysis [11] so this research can pave the way for developing fast and accurate methods for predicting the deformations and its resulting effects on the clearances and thus on volumetric efficiency.

1.6. Methodology

ANSYS simulation software will be used to numerically investigate the complex flow field inside the Roots blower. Its flexible interface allows for integration of the custom meshes from SCORG mesh generator software.

In the pre-analysis phase the mathematical model (governing equations and boundary conditions) is defined, as well as the numerical solution procedure using the Finite volume method. FVM converts the integral form of governing equations to a large set of non-linear algebraic equations relating cell-centre values. We solve this non-linear system of algebraic equations by linearizing non-linear terms about guess values. Linearization and discretization schemes are put together into an algorithm for iterative solution which keeps tweaking the guess values using the linearized algebraic equations until imbalances are below tolerance. Finite volume method is preferred over Finite element method for CFD applications because it conserves quantities in a discrete sense (for each control volume) by using the control volume balance for each cell. Thus, conservation is built into the method.

The analysis phase is where the CFD simulations are done to test the numerical methodology. This phase is divided into two separate phases. The first phase is to perform non-conjugate CFD simulations of the flow domain and define walls as adiabatic in order to calibrate the axial gap. The approach is to neglect the rotor deformations and assume rigid compressor elements. So the tip gap in the computational domain is constant which is not the case in the real machine. To account for the changes in leakage flow in the clearance gaps due to thermal deformations and consequently the changes in inflow in the experimental setup, axial gap needs to be adjusted to match the measured flow at operating test conditions. In the second phase heat transfer to solid components of rotors and casing is included. The goal is to perform conjugate heat transfer simulation and calculate the temperature fields in the computational domain.

Post-processing will be performed with ANSYS CFD-Post program to postprocess the data and show modelling results. CFD-Post is a full-feature post processor and has more capabilities than the inbuilt post-processor inside Fluent.

After developing the methodology, the validation is be performed to check whether the mathematical model is the right representation of the physical problem and for this we need to check against experimental data. The physical setup is interrogated directly by using Infrared thermography.

1.7. Customized meshes with SCORG

Internal flow inside the blower is highly transient and to predict its characteristic under these conditions we need to capture the mesh deformation. To allow for this deformation, due to intermeshing of the rotors, we need to employ the moving mesh technique. This technique is used by popular CFD software packages like ANSYS Fluent and CFX.

Due to limiting options offered by the moving mesh techniques in these commercial CFD solvers, customized meshes are needed. Options like layering, smoothing and remeshing are just too limited to tackle the most challenging dynamic mesh problems like in the positive displacement machines where working medium is displaced during simulation. Kovačević [14] pioneered and implemented algebraic method to generate customized block-structured deforming mesh for twin screw rotors. This allowed engineers to analyse this highly transient flow dynamics in positive displacement machines. This method is implemented in SCORG and classified as Rotor-Casing method. Rane [5] improved on this and developed a new approach which is classified as Rotor-Casing. For more details about the new developments in the algebraic method SCORG employ for mesh generation, see [12], [13]. The new developments allowed for conformal mesh interface between the dynamic rotor domains which will be used in this research.

Customized meshes from SCORG can be used with commercial CFD codes like Star CCM+, ANSYS Fluent and CFX which all have flexible interfaces to allow for customized grid integration. The purpose of the mesh generator is to decompose the flow domain into elements. It generates 2D mesh with quadrilateral elements and extrudes it to form a 3D mesh for initial rotor position. Then it generates pre-processor input files for selected CFD solver for each timestep. It employs algebraic and hybrid differential methods for mesh generation. Apart of the main functionality to construct deforming meshes in the rotor domain of a positive displacement machines, the software includes additional modules for handling rotor profiles, extracting profiles coordinates from CAD models and generating the pre-processing setup routines for selected commercial CFD solvers [15].

2. MATHEMATICAL MODEL

In this chapter the mathematical modelling will be presented.

2.1. Conservation laws for a control volume

Basic laws of fluid mechanics are: mass conservation law, conservation of momentum and energy conservation law. These laws are described by equations which govern the fluid flow and are called governing equations. They can be written in Lagrangian or Eulerian frame of reference. Lagrangian frame of reference moves with the flow field so we follow individual particles. Using the Lagrangian approach we can monitor trajectories of individual particles and calculate changes in different physical properties or forces which the particle experiences while galloping through the computational domain. In this case the conservation laws are applied in a coordinate system which is attached to the particle itself. This approach is often used in spray modelling and is also known as discrete phase approach. In Eulerian frame of reference we follow fixed points in space through which the fluid flows so we need to transform the basic laws of motion which are written in Lagrangian frame of reference. In this research, Eulerian approach is employed as we consider the working medium as a continuum.

2.1.1. Mass conservation equation

The mass conservation law states that the net mass crossing the boundary of a control volume must be balanced by an accumulation or depletion of mass in that control volume For compressible flow, the mass can increase or decrease within the control volume.

Mass conservation equation or equation of continuity is mathematically defined as:

$$\frac{\partial \rho}{\partial t} + \frac{\partial (\rho v_j)}{\partial x_j} = 0 \qquad \textbf{(2.1)}$$

2.1.2. Momentum conservation equations

The momentum conservation equations are derived from the second Newton's law of motion. It states that the sum of the forces acting on a fluid particle is equal to the mass of the element multiplied by its acceleration. The formulation below is a 3D transient formulation of the Navier Stokes equations for compressible flow in Eulerian frame of reference:

$$\frac{\partial (\rho v_i)}{\partial t} + \frac{\partial (\rho v_j v_i)}{\partial x_j} = \frac{\partial}{\partial x_j}\left(-p\delta_{ji} + \Sigma_{ji}\right) + \rho f_i \qquad \textbf{(2.2)}$$

where Σ_{ji} is the symmetric tensor of viscous stresses: Newton's law of viscosity establishes a linear connection between the viscous stress tensor and the elastic stress tensor so the total stress tensor is given by:

$$\sigma_{ji} = -p\delta_{ji} + \Sigma_{ji} \tag{2.3}$$

where δ_{ji} is the unit tensor.

Assuming fluid isotropy, viscous stress tensor can be modelled by the expression:

$$\Sigma_{ji} = \mu\left(\frac{\partial v_j}{\partial x_l} + \frac{\partial v_i}{\partial x_j}\right) + \left(\mu_v - \frac{2}{3}\mu\right)\frac{\partial v_k}{\partial x_k}\delta_j \tag{2.4}$$

The influence of volume viscosity is only significant in flows with significant density gradients, like in explosions or shock waves. Volume viscosity of monoatomic gases is equal to zero and in flows where the rate of change of volume of fluid particles (i.e. fluid density) is small the coefficient of volume viscosity can be omitted [16]:

$$\Sigma_{ji} = \mu\left(\frac{\partial v_j}{\partial x_i} + \frac{\partial v_i}{\partial x_j}\right) - \frac{2}{3}\mu\frac{\partial v_k}{\partial x_k}\delta_{ji} \tag{2.5}$$

The equations 2.1 and 2.3 are valid for compressible flow and they can be simplified further for incompressible flow. This will not be explored in this thesis.

2.1.3. Energy conservation equation

The energy conservation equation is derived from the first law of thermodynamics which states that energy can't be produced or destroyed, just converted from one form to another. The change in energy over time is equal to the sum of the work done and the thermal energy generated:

$$\frac{\partial(\rho c_v T)}{\partial t} + \frac{\partial(\rho c_v v_j T)}{\partial x_j} = -p\frac{\partial v_j}{\partial x_j} + \Sigma_{ji}\frac{\partial v_i}{\partial x_j} + \frac{\partial}{\partial x_j}\left(\lambda\frac{\partial T}{\partial x_j}\right) + \phi_v \tag{2.6}$$

It can be seen from the Navier-Stokes equations that density can affect the flow if the flow is compressible. This leads to obligatory inclusion of Energy conservation equation for obtaining temperature field even if the flow is adiabatic.

In compressible flow all three governing equations are coupled through a thermodynamic state and need to be solved together. To close the system and solve for all the unknowns an additional equation needed.

In this thesis the working fluid is air and it will be considered as an ideal homogenous gas. Density of ideal gasses is calculated using the equation of state which is a thermodynamic equation that connects the variables that describe the state of matter under given physical conditions:

$$\rho = p \cdot \frac{M}{RT} \tag{2.7}$$

where p is the pressure field, M is the molar mass of the fluid, R is the gas constant, and T is the temperature field.

For incompressible flows, the density is assumed to be constant so the energy equation ceases to be coupled to the continuity and the momentum equations. Temperature distribution can be obtained separately by plugging-in the velocity and pressure values in the energy equation.

2.1.4. *General scalar transport equation*

The equations presented above can all be considered as a specific case of a generalized equation called the scalar transport equation. It describes how a general property ϕ is transported:

$$\underbrace{\frac{\partial \rho \phi}{\partial t}}_{\text{Transient term}} + \underbrace{\nabla \cdot (\rho \vec{u} \phi)}_{\text{Convection term}} = \underbrace{\nabla \cdot (\Gamma \nabla \phi)}_{\text{Diffusion term}} + \underbrace{S_\phi}_{\text{Source term}} \tag{2.8}$$

The temporal derivative in the transient term represents the potential of the control volume to accumulate the general property ϕ. The convection term accounts for the transport of ϕ due to existence of the convective velocity. The diffusion term represents the transport of ϕ due to existing gradients. The source term accounts for the local production or destruction of the general property ϕ.

This generic representations of governing equations allows for a systematic approach in computer simulations. There is no need to write all the equations in code separately. Instead, ϕ can be assigned different values according to the type of equation which needs to be solved.

2.2. Turbulent flow

Turbulence is extremely unsteady, irregular and irreversible phenomena in which transporting properties fluctuate in time and 3D space which means that a very small distance between computational points is required. Typical techniques for solving turbulence numerically can be divided into two groups:

- Turbulence modelling (RANS)
- Turbulence simulation (DNS, LES)

In which:

DNS: Direct Numerical Simulation

LES: Large Eddy Simulation

RANS: Reynolds-Averaged Navier-Stokes

Solving for the unsteady governing equations and capturing turbulence in all its scale (from smallest to largest eddies) with DNS is computationally extremely expensive approach. 3D stochastic and irregular motion means that the turbulent simulation must have extremely fine grids. These large requirements entail enormous computational power so additional modelling is the preferred option for real applications. Full resolving DNS remains to be extremely time-consuming for Reynolds numbers greater than 10^4 [17]. As the full spectrum of eddys, which are resolved by the brute-force in DNS, are usually not needed for most applications, a popular alternative is less expensive LES. It has large scale resolution which means that only the large and most energetic eddies are computed directly while the effects of the smaller ones are modelled. Capturing only the biggest of eddies is often enough and it puts less demand on the numerics than the DNS. It also requires less modelling effort than the RANS approach. There are also hybrid methods which combine LES and RANS.

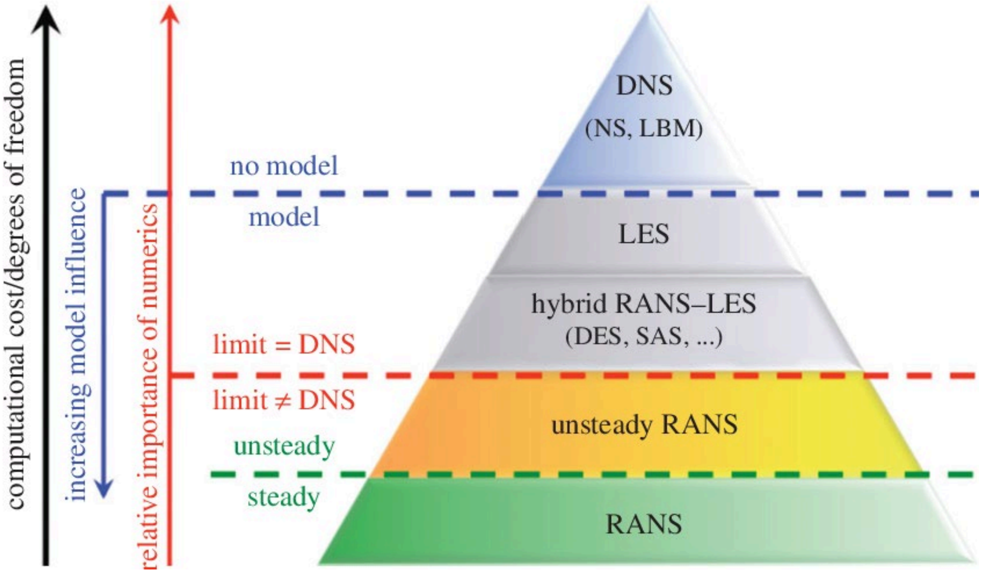

Figure 7 Difference between RANS, LES and DNS [18]

This thesis will employ turbulence modelling because solving for turbulence is still too computationally expensive. Overview of the mentioned approaches is given in Figure 7.

2.2.1. Turbulence modelling with RANS

Using two equation RANS turbulence models is possible due to statistical averaging which in most engineering cases is more than enough as engineers are often interested in integral values. This significantly simplifies the problem of numerically solving for the governing equations because the spatial and temporal discretization steps no longer have to be so small. The averaging of non-linear term produces correlations which have to be modelled, like Reynolds stress tensor:

$$R_{ij} = -\rho\overline{u_i'u_j'} = \mu_T\left(\frac{\partial\bar{u}_i}{\partial x_j} + \frac{\partial\bar{u}_j}{\partial x_i}\right) - \frac{2}{3}\mu_\mathrm{T}\frac{\partial\bar{u}_k}{\partial x_k}\delta_{ij} - \frac{2}{3}\rho k\delta_{ij} \tag{2.9}$$

To close the system of averaged NS equations, Reynolds stresses need to be modelled and this is an extremely difficult task. The two models which close this system are Eddy Viscosity Models and Reynolds-Stress Models. Eddy Viscosity Models employ Boussinesq hypothesis and model the Reynolds stresses using turbulent viscosity. There are several sub models and each of them calculates turbulent (or eddy) viscosity differently. Reynolds-Stress Models calculate transport equations for Reynolds stresses.

2.2.2. k-ω SST turbulence model

k-ω SST with automatic wall functions is one of the most reliable RANS turbulence models. It was developed by Menter to make standard k-ω more accurate for a wider varieties of fluid flows. The model tries to mitigate drawbacks of individual k-ω and k-ε by combining them together by using a blending function. It uses standard SST model for use near walls and the standard k-ε in free stream.

It is the most prominent two-equation model and it gives high accurate predictions of the onset and the amount of flow separation so it is proper for simulating the effects of the adverse pressure gradients in the flow exiting the clearance gaps [19], [20]. Other two-equation models over predict turbulent stresses in wake of separated flows which is important in flow regimes in which the boundary layer is submitted to strong adverse pressure gradients. In the clearance gap pressure decreases until the flow reaches the throat after which it starts to increase, resulting in an unfavourable pressure gradient.

As an Eddy viscosity sub model, k-ω turbulence model is coupled to governing equations of fluid flow by turbulent viscosity μ_T which is defined as a function of:

$$\mu_T = f\left(\frac{\rho k}{\omega}\right) \tag{2.10}$$

The model solves additional two transport equations for Turbulent kinetic energy k and Specific dissipation rate ω:

$$\frac{\partial}{\partial t}(\rho k)+\frac{\partial}{\partial x_i}(\rho k u_i)=\frac{\partial}{\partial x_j}\left(\Gamma_k\frac{\partial k}{\partial x_j}\right)+\tilde{G}_k-Y_k+S_k \quad \textbf{(2.11)}$$

$$\frac{\partial}{\partial t}(\rho\omega)+\frac{\partial}{\partial x_i}(\rho\omega u_i)=\frac{\partial}{\partial x_j}\left(\Gamma_\omega\frac{\partial\omega}{\partial x_j}\right)+G_\omega-Y_\omega+D_\omega+S_\omega \quad \textbf{(2.12)}$$

The effective diffusivities for the model are given by:

$$\Gamma_k=\mu+\frac{\mu_t}{\sigma_k} \quad \textbf{(2.13)}$$

$$\Gamma_\omega=\mu+\frac{\mu_t}{\sigma_\omega} \quad \textbf{(2.14)}$$

Production of k is defined in the same way as in the standard k-ω model and is evaluated with the Boussinesq hypothesis:

$$G_k=\mu_t S^2 \quad \textbf{(2.15)}$$

Production of ω differs from the standard model in how the coefficient α is defined:

$$G_\omega=\frac{\alpha}{\nu_t}G_k \quad \textbf{(2.16)}$$

Y_k and Y_ω in equation 2.11 and 2.12 represent dissipation:

$$Y_k=\rho\beta^* f_{\beta^*}k\omega \quad \textbf{(2.17)}$$

$$Y_\omega=\rho\beta f_{\beta^*}\omega^2 \quad \textbf{(2.18)}$$

the main difference from the standard model is that f_{β^*} is constant and equal to 1:

$$Y_k=\rho\beta^* k\omega \quad \textbf{(2.19)}$$

$$Y_\omega=\rho\beta\omega^2 \quad \textbf{(2.20)}$$

Lastly, the equations of the standard k-ε need to be transformed to blend into k-ω which leads to introduction of a cross-diffusion term D_ω:

$$D_\omega=2(1-F_1)\rho\sigma_{\omega,2}\frac{1}{\omega}\frac{\partial k}{\partial x_j}\frac{\partial\omega}{\partial x_j} \quad \textbf{(2.21)}$$

For more details about the model's constants and blending functions, see [21], from where these equations were taken. Blending functions are responsible for gradual transition from the standard k–ω model near the wall to a high Reynolds number version of the k–ε model in the outer portion of the boundary layer.

2.3. Conjugate heat transfer

The main mechanisms by which heat is transferred are conduction, convection and radiation. Conduction and convection are similar mechanisms. They both need an energy carrier, a particle. The only difference between the two mechanism is that in conduction the particles are bound to their atomic position while in convection they can move freely. Radiation does not need the existence of matter as a mediator. The carrier is an electromagnetic wave that can propagate through vacuum. In this thesis, radiation will be neglected.

2.3.1. Conduction heat transfer

Conduction of heat through a homogeneous opaque solid happens from one end to the other under the influence of a temperature gradient without noticeable particle motion. The movement takes place intermolecularly. The physicality of this mechanism of heat transfer lies in the transfer of kinetic energy from one molecule to another adjacent molecule by intermolecular vibration.

The heat flux between two bodies is proportional to the temperature difference between them. The heat flux according to Fourier's law:

$$q_j = -\lambda \cdot \frac{\partial T}{\partial x_j} \tag{2.22}$$

where q is the heat flux density, λ is the thermal conductivity of a material, and $\partial T/\partial x_j$ is the temperature gradient. The negative sign is needed to switch the heat flux density vector to the direction opposite of temperature gradient because heat transfer always happens towards the area with lower temperature.

The relationship between thermal conductivity, conductivity and specific heat capacity is:

$$\lambda = a \cdot \rho \cdot c_p \tag{2.23}$$

Conduction heat transfer equation is derived from the energy conservation equation by eliminating the convective term:

$$\rho c_p \frac{\partial T}{\partial t} - \frac{\partial}{\partial x_j}\left(\lambda \frac{\partial T}{\partial x_j}\right) = \phi_v \tag{2.24}$$

where ρ is the density, c_p the specific heat capacity, λ the thermal conductivity and ϕ_v is a volumetric heat source.

2.3.2. Convection heat transfer

In addition to intermolecular motion at atomic level, convection heat transfer additionally takes place by mixing differently tempered fluid particles. The mixing happens on macro-scale and can be natural, forced or mixed depending on the main forces that cause fluid motion.

Natural convection takes place if the motion of a fluid is conditioned only by a difference in particle density. This difference may be due to uneven temperature distribution or differences in concentrations in the mixture. The heterogeneity of mass forces (buoyancy) over the observed control volume allows fluid flow. Forced convection occurs when the motion of a fluid is conditioned artificially with imposed external pressure difference, e.g. fan.

Newton's law of cooling states that the rate of heat transfer is proportional to the temperature difference between a surface and the fluid surrounding it:

$$\frac{\partial Q}{\partial t} = \alpha \cdot A \cdot (T_s - T_\infty) \qquad \textbf{(2.25)}$$

where Q is the thermal energy, T_s is the surface temperature, T_∞ is the fluid temperature, A is the surface area, and α is the heat transfer coefficient.

2.3.3. Boundary conditions

Boundary and initial conditions are needed to fully define the problem on a differential level. With given initial and boundary conditions, the PDE system presented above unambiguously describes the boundary value heat transfer problem of Newtonian ideal gas flow. Specifically, a boundary condition defines the behaviour of a function on the boundary while an initial condition defines the behaviour at initial time.

2.3.3.1. Thermal boundary conditions

The thermal boundary conditions which will be applied at the outer surfaces in the analysis to provide good relationship between the numerical model and measurements are convection and adiabatic boundary conditions.

Adiabatic boundary condition is a special case of the second kind boundary condition which prescribes the heat flux at the boundary. As it is adiabatic the heat flux at the boundary is set to zero as show in the equation below. In other words, there is no heat transfer across this boundary.

$$\frac{\partial T}{\partial x_j} = 0 \qquad \textbf{(2.26)}$$

Convection boundary condition is a boundary condition of the third kind and it essentially represents the Newton's law of cooling:

$$q = \alpha \cdot (T_s - T_\infty) \tag{2.27}$$

2.3.3.2. Coupled thermal boundary condition

In a conjugate heat transfer analysis boundary condition of the fourth kind is prescribed at the mapped fluid-solid interfaces to allow for transfer of heat energy from fluid to solid. This coupled boundary condition binds the solid and fluid solution so no constraints need to be made at these interfaces. Interface is a 2D surface and it is not capable of accumulating energy so two conditions have to be met in fluid-solid coupling:

$$T_f = T_s \tag{2.28}$$

$$\left(\lambda \frac{\partial T}{\partial x_j}\right)_f = -\left(\lambda \frac{\partial T}{\partial x_j}\right)_s \tag{2.29}$$

where the subscripts indicate quantities at the solid and fluid side of the interface.

The system of governing equations presented above is a system of non-linear partial differential equations and for the most part, it will not be possible to find an analytical solution to this system. For solving this system of PDEs we need to apply numerical methods and solve it approximately. In this work the finite volume method will be employed by using a segregated PISO solver. Discretized integral forms of the previously mentioned equations are used in solving.

3. NUMERICAL MODEL

The numerical technique which will be used to solve the governing equations of fluid flow is the finite volume method (FVM). The basic idea of FVM is to divide the flow domain into finite volumes (control volumes) and apply conservation to each finite volume. Finite volume balance for each cell is done by using the integral form of the governing equations. This results in a set of algebraic equations. The main difference from Finite element method is in how this system of algebraic equations is derived. In FEM it is done by going from the weighted integral form an using polynomial interpolating. The objective of both discretization techniques is to transform the generic scalar transport equation into linear system of algebraic equations.

3.1. Domain discretization

A mesh divides geometry into many discrete elements which are then used by the CFD code to construct cells or control volumes (Figure 7 [22]). Fluent is a cell centred solver and the number of elements is the same as the number of cells and can be used interchangeably. This is not the case with CFX where the number of cells is equal to the number of nodes. Elements are composed of edges, faces and nodes and can take the same form as cells showed in the subheading 3.2.2.

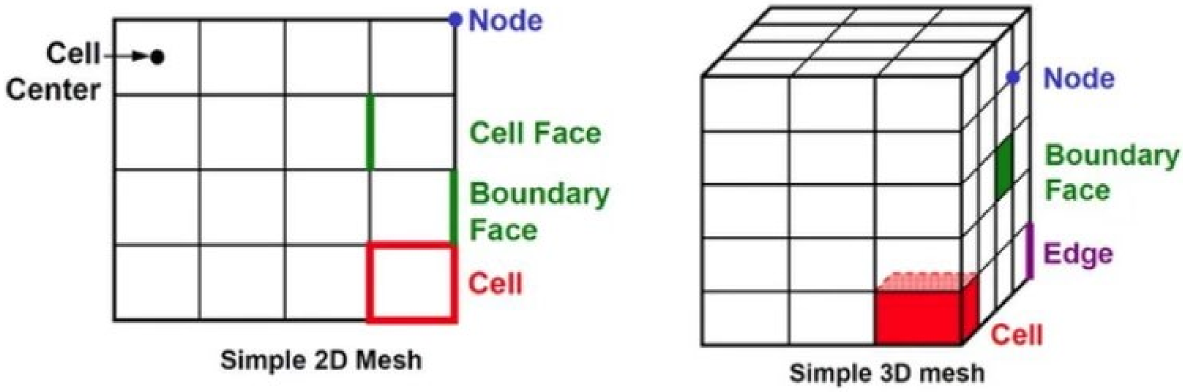

Figure 8 Mesh terminology [22]

By spatial discretization, we simplified the problem of determining the value of unknowns in the centres of control volumes.

3.1.1. Structured and unstructured meshes

Depending on how mesh points are connected, mesh systems can be divided into structured and unstructured [23]. The only difference between the structured and unstructured mesh systems is simply in how the data is stored.

Structured grid systems have fixed topology and are divided into body-fitted and multi-block meshes. Body-fitted mesh follows contours of physical domain which means that faces of control volumes are aligned with geometry and with the flow. This guarantees solution accuracy. The main issue with this mesh system is that it can’t be used for highly complex geometries because it forces topology on the mesh. Multi-block mesh is better in that regard because it offers more flexibility. All nodes need to be mapped to a cartesian coordinate system by conformal mapping. Nodes are expressed by integer indices (i, j, k) which easily imply connectivity and identification of nodes. This simplifies programming and demands less memory allocation because it is easy to loop through neighbours due to regular patterns.

Unstructured mesh system store an integer index for each node and connectivity table which stores indices of the neighbouring cells. Their structure is arbitrary as nodes numbered randomly without using i, j, k indexing. Essentially, each unstructured node class, which will be used as a blueprint for creating node objects, has to have more attributes than their structured counterpart. These attributes should include connectivity lists, coordinate lists and a single integer index which will be unique. The implications on the memory utilisation are far higher memory requirements.

Fluent is unstructured finite volume code and it can handle both unstructured and structured meshes. Mesh topology can change during calculation and the solver can do flux reconstruction on each face whatever the shape of the cell is.

3.1.2. Cell types

The computational domain is filled out with 3D control volumes (or cells) which represent computational points. These cells can be divided by shapes depending if the analysis is 2D or 3D. Figures below show the basic 2D and 3D cell types in CFD meshing. There are two basic 2D types: triangle and quadrilateral. 3D types are: tetrahedron, hexahedron, pyramid and polyhedron. Careful selection is important for both computational efficiency and solution accuracy as mesh is directly related to how the matrix of our system will look like. Polyhedral cells are great for meshing complex geometries like blades of a turbine.

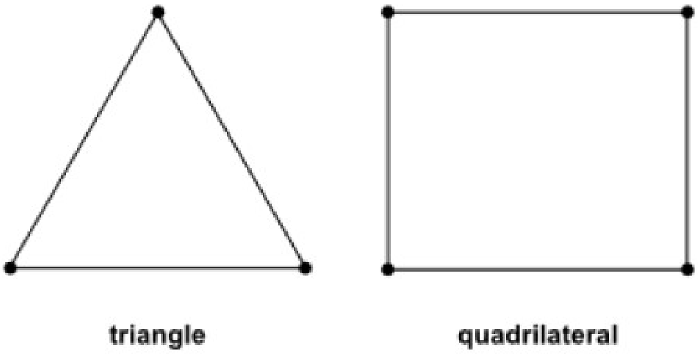

Figure 9 2D Control volume types [24]

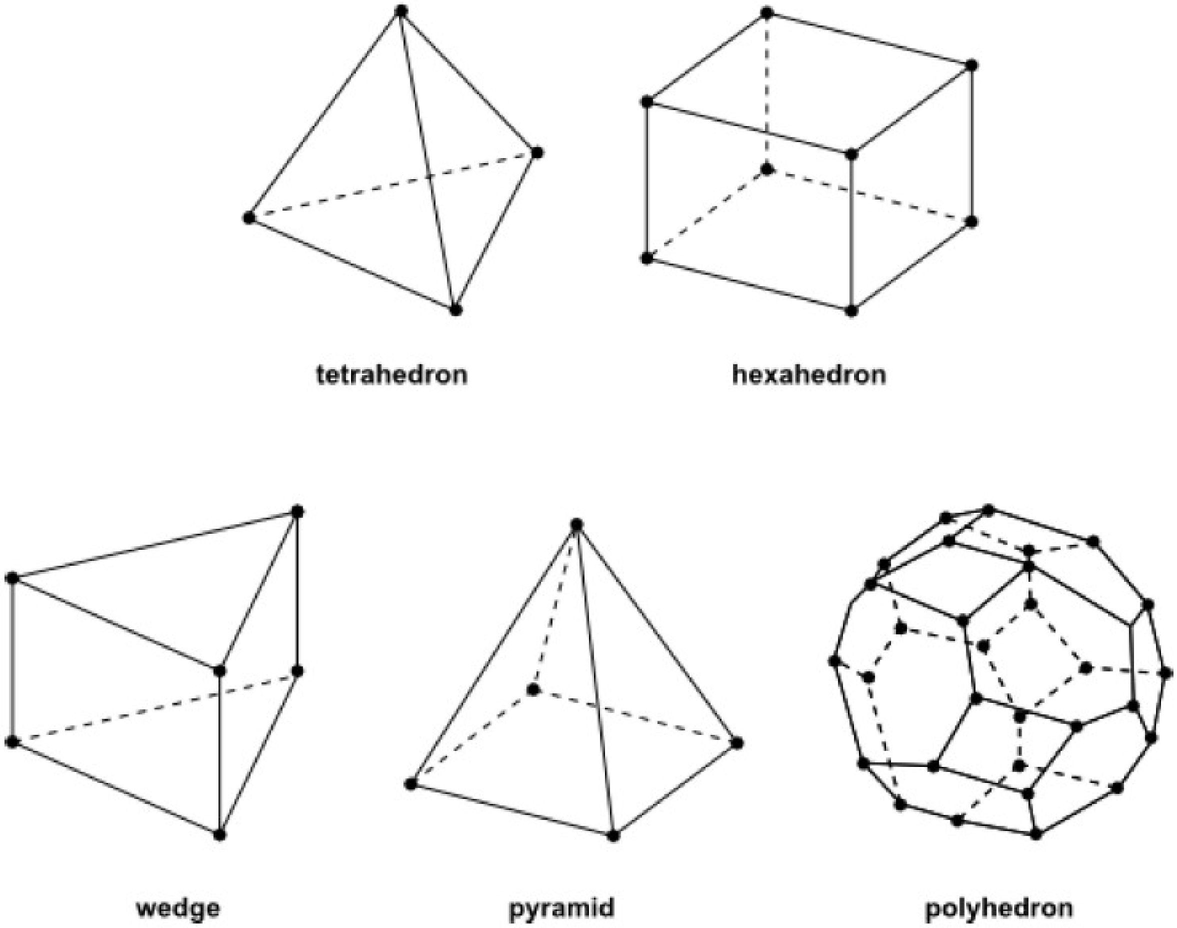

Figure 10 3D Control volume types [24]

A mesh divides a geometry into many elements. These are used by the CFD solver to construct control volumes.

3.2. Time discretization

Time integration of integral governing equations is carried out with an implicit first order time marching method.

Time marching in the fluid domain is restricted by the CFL (Courant–Friedrichs–Lewy) condition which states that the distance that any information travels during a timestep in a mesh must be lower than the mesh spacing. Basically, it is a fraction of two lengths; distance the fluid particle will travel over a timestep and the length of a cell:

$$\frac{\Delta t_f V}{\Delta x_f} < 1 \tag{3.1}$$

If the Courant number is less than 1, then the fluid particle will move from one cell to another within a timestep. However, if it is more than 1 the particle can move through many cells within a timestep which can affect convergence negatively.

Time marching in the solid domain can be expressed by Fourier number that characterizes transient heat conduction. It is the ratio of the rate of heat conduction and the rate of thermal energy stored in a body:

$$\frac{\Delta t_a \alpha}{\Delta x_s^2} < 0.5 \tag{3.2}$$

the dominant time scales for diffusive phenomena in the solid domain and convective phenomena in the fluid are quite different. As demonstrated in [25] the ratio of time scales between the solid conduction and fluid convection can be around 10000. They considered a case with a convection speed of V = 300 m/s, steel as solid material (specific heat 465 J/(kgK), density 7800 kg/m^3, thermal conductivity 54 W/(mK). The mesh spacing is 0.001 m. The ratio then becomes:

$$\frac{\Delta t_s}{\Delta t_f} \approx 10000 \tag{3.3}$$

In CHT studies it is desirable to have a larger time step in solid zones, while maintaining a smaller time step in fluid zones. This increases the speed at which the solid heat transfer reaches steady-state without compromising the solution accuracy of the fluid flow [24].

Fluent allows for different time step size to be specified for solid zones which will be used in this work to perform time scale analysis.

3.3. Discretization of governing equations

To allow for a numerical solution, governing equations must be discretized both in space and time. The domain discretization is achieved through the use of the finite volume method. As mentioned before, discretized integral forms of these equations are applied to finite volumes in the computational domain. Integral forms of governing equations can be applied to any arbitrary shape of a control volume within the computational domain. As Fluent uses a cell-centre scheme, flow variables are stored in the cell centres.

Each integral algebraic equation will relate the values at the centre of the control volume, which are at the centre of gravity of the volume, to the values at the centres of adjacent cells. An integral equation is placed on each cell and volume integrals are transformed into surface integrals. Then, the surface integral needs to be turned into a finite summation over the boundary surfaces. This is done by defining an average value of the flow properties. By interpolating the values in the centres of adjacent cells, the values on the control surfaces of the cell are obtained. For boundary cells, boundary condition values are extrapolated.

With this discretization procedure, we introduce a discretization error into the solution. We can reduce this error by refining the mesh, that is by increasing the number of control volumes in the mesh or by increasing the order of interpolation.

The gradients were discretized by the least squares method while the convective terms of transport equations were discretized by the upstream scheme of the second order of accuracy.

Since the equation of conservation of momentum has a nonlinear term we have to linearize it around the guess values and then we change this value by an iterative procedure until the solution converges. The Newton-Rhapson method can be used for linearization. By linearizing the system of algebraic equations, we introduce a linearization error into the solution.

This thesis will employ a segregated solver which numerically solves the partial differential equations one at a time. To solve this problem the momentum equation needs to be coupled to the continuity equation in so called pressure-velocity schemes. This is done by solving for the pressure-correction equation. The pressure-velocity coupling scheme scheme which will be used here is PISO. PISO is an extension of the SIMPLE algorithm and was developed for solving unsteady compressible flow, The scheme uses following steps:

- Use the available pressure field from previous time-step or set up an initial pressure field p^*.
- Solve the discretized momentum equation to obtain v_1^*, v_2^*, v_3^*.

- Compute the mass fluxes at the cells faces.
- Solve the correction equations to obtain p', v_1', v_2', v_3'.
- Update cell-centred values with: $p = p^* + p'$, $v_1 = v_1^* + v_1'$, $v_2 = v_2^* + v_2'$, $v_3 = v_3^* + v_3'$.
- Return to pressure correction if convergence is not reached
- Solve the energy equation for temperature T.
- Begin the next iteration by setting $p = p^*$.

Under-relaxation factors are used to prevent divergence. This will dampen the oscillation in the P-V coupling and stabilise the convergence.

3.4. Dynamic mesh

The dynamics mesh option which will be used here is the smoothing method with in-cylinder options. It adjust the mesh of an area by deforming boundaries while keeping the topology constant, so there is no change in the number of nodes or connections between them.

Mesh generation software SCORG is used for generating custom deforming meshes to overcome limitations of commercial CFD software packages . The program generates 2D mesh with quadrilateral cells and extrudes it to form a 3D mesh for initial rotor position. Then, it generates pre-processor input files for selected CFD solver for each timestep. These are text files containing information about node indices and positions. User Defined Functions will be used to extract this information and pass it to the solver. Solver needs these input files during computations to translate the nodes. There is an option for generating a non-conformal mesh interface as well as a conformal interface.

3.4.1. Integration of custom meshes with Ansys software

Fluent uses User Defined Functions in order to read custom mesh files and transition the nodes with each timestep. Visual Studio IDE was used to externally compile UDF source code written in C and build a shared library object file which is then loaded into FLUENT. This way UDFs can be called on demand or during the execution of the CFD code. An alternative approach is to use interpreted UDFs which are executed on an internal interpreter or emulator whenever called by the solver so they do not require C compiler. This has a performance penalty due to the additional operation which has to be performed during execution.

Code written in C cannot be used in CFX in order to read the mesh files generated by SCORG as CFX implements a different interface called Junction Box Routines. It allows for integration of user-defined subroutines written in Fortran. These subroutines need to be compiled as well in order to build a shared library of subroutines which will be linked to the CFX solver during calculation.

3.4.2. User Defined Nodal Displacement

User Defined Functions allow for customization of the solver and can be dynamically loaded while the solver is iterating. They are written in C programming language and are implemented as macros. This thesis will utilize already predefined Fluent macros:

- DEFINE_ON_DEMAND,
- DEFINE_GRID_MOTION

to allow for integration of custom meshes from SCORG.

DEFINE_ON_DEMAND allows for asynchronous execution of a UDF rather than calling it automatically during calculation.

DEFINE_GRID_MOTION is available while the solver is calculating. It will be used to control the motion of each node independently and update their position using linear interpolation between the mesh files generated by SCORG.

The general format for an already predefined macro function is the macro name followed by arguments in the parentheses. First argument is the name of the UDF and the rest of the arguments are passed-in variables.

When the mesh is loaded into the solver, Fluent uses internal data structures to:

- assign an order to the nodes in a mesh by initializing indices in memory.
- assign coordinate list to nodes and maintain mesh connectivity by initializing connectivity lists.

The initialized indices are stored in memory in an unstructured format randomly and they do not match the index numbers specified in the pre-processor mesh files. These indices need to be aligned to allow for mesh movement with each consecutive timestep. This process is called 'Node mapping' and it reads the information about node x, y, z coordinates to perform an operation which will relate the node data from SCORG to the node data from loaded mesh. The criteria for determining this relation is the shortest distance between the nodes from SCORG mesh files (x_i, y_i, z_i) and the nodes from the loaded mesh (x_j, y_j, z_j) [26]:

$$d = \sqrt{\left(x_j - x_i\right)^2 + \left(y_j - y_i\right)^2 + \left(z_j - z_i\right)^2} \qquad \textbf{(3.4)}$$

after successful node mapping each node loaded into system memory will be matched with the SCORG mesh files by the information stored in User-Defined Node Memory (UDNM). There are 4 locations in User Defined Memory: the 1st location stores the index and the other 3 store coordinates of the mapped node. This process is executed asynchronously with DEFINE_ON_DEMAND macro in parallel MPI mode.

DEFINE_GRID_MOTION UDF is used by the solver while iterating to access the mapped nodes in memory and update their position using linear interpolation if needed. It controls the motion of the nodes inside the mesh. Mesh files are generated for 180 rotor positions with an angular step size of 1°. If the timestep is smaller than 1° and the external mesh files do not exist for the current crank angle while the solver is iterating, then linear interpolation of x, y, z coordinates will be performed in the UDF between the previous crank angle integer and the following crank angle integer. If the mesh files exist for the current crank angle there is no need for linear interpolation. Then, the solver will just read the node positions from external mesh file for this crank angle and translate the mesh nodes accordingly. This process is shown in the Figure below [27].

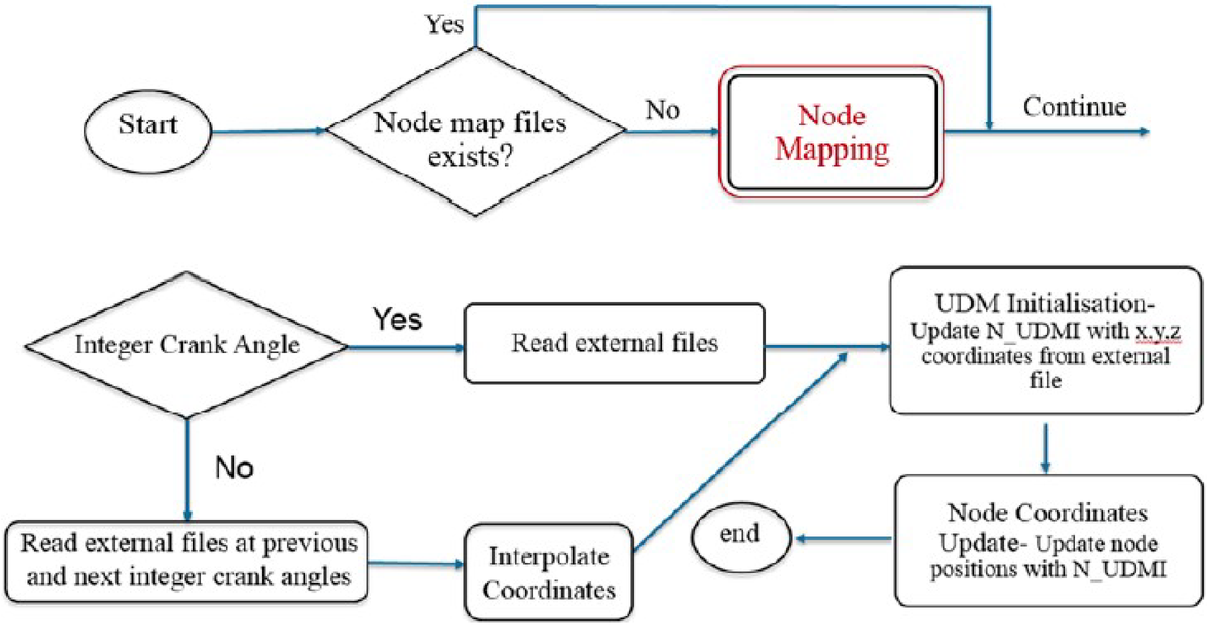

Figure 11 Flow chart of DEFINE_GRID_MOTION UDF macro [27]

This UDND routine was developed by Nausheen [26] and it will be used to allow for grid deformation in Fluent. In the next chapter, the solver will be setup for calibration of axial clearance gap.

4. GAP CALIBRATION

This chapter discusses the methodology and results obtained with the non-conjugate CFD simulation. First, the computational domain and case setup are presented. This is followed by the discussion of numerical solution and comparison against experimental data.

The rise of temperature in rotors and casing affects internal clearances and thus it causes changes in volumetric efficiency. if compression is 100% efficient, it means that all of the air coming into the inport will traveling through the system and leave through the outport. This is not the case as there are internal clearances between the rotors and the casing. Air will flow form the high pressure region to the low pressure region causing losses. This research assumes rigid rotor and casing elements so the interlobe and the tip gap will be constant. The changes in the gap size, and consequently mass flow rate, due to thermal deformations in the real machine are taken into account with the process of calibrating the axial clearance gap.

The axial gap is scaled at different operating conditions to account for fixed interlobe and tip gap size. Table 1 [28] shows the main parameters of the blower which will be investigated.

Table 1 The main parameters of the Blower [28]

Items	Specification	Items	Specification
Diameter of the rotor [mm]	101.3	Tip gap [mm]	0.1
Axis distance [mm]	63.12	Interlobe gap [mm]	0.17
Rotor length [mm]	50.5	Axial gap [mm]	0.15
Displacement volume [l/rev]	0.4618	Width of tip step [mm]	6.4
Diameter of the rotor [mm]	101.3	Tip gap [mm]	0.1

4.1. Computational domain

4.1.1. Dynamic mesh

The mesh shown on the pictures below is generated in SCORG together with 180 pre-processor text files which contain the node positions for each angle integer. The total number of nodes in the computational domain are: 573500. The same number of nodes are written in the pre-processor text files. DEFINE_ON_DEMAND UDF was executed before the run to map the nodes and create the mapping scheme inside the User Defined Node Memory. Figure 12 shows the non-conformal mesh while Figure 13 shows conformal mesh generated in SCORG. Conformal mesh option was the latest addition to SCORG software and generally this algorithm provides better quality mesh. However, the rack curve that is generated for these types of machines is very steep and the algorithm experiences difficulties in providing the high quality mesh for all rotor angles. The most problematic angle for the conformal mesh generation is 45° as highly skewed cells get produced. To avoid this the initial approach was to use the non-conformal mesh as the accuracy and validity of simulations depend on the amount of cells and the quality of these cells. Grid independency study wasn't conducted in this thesis.

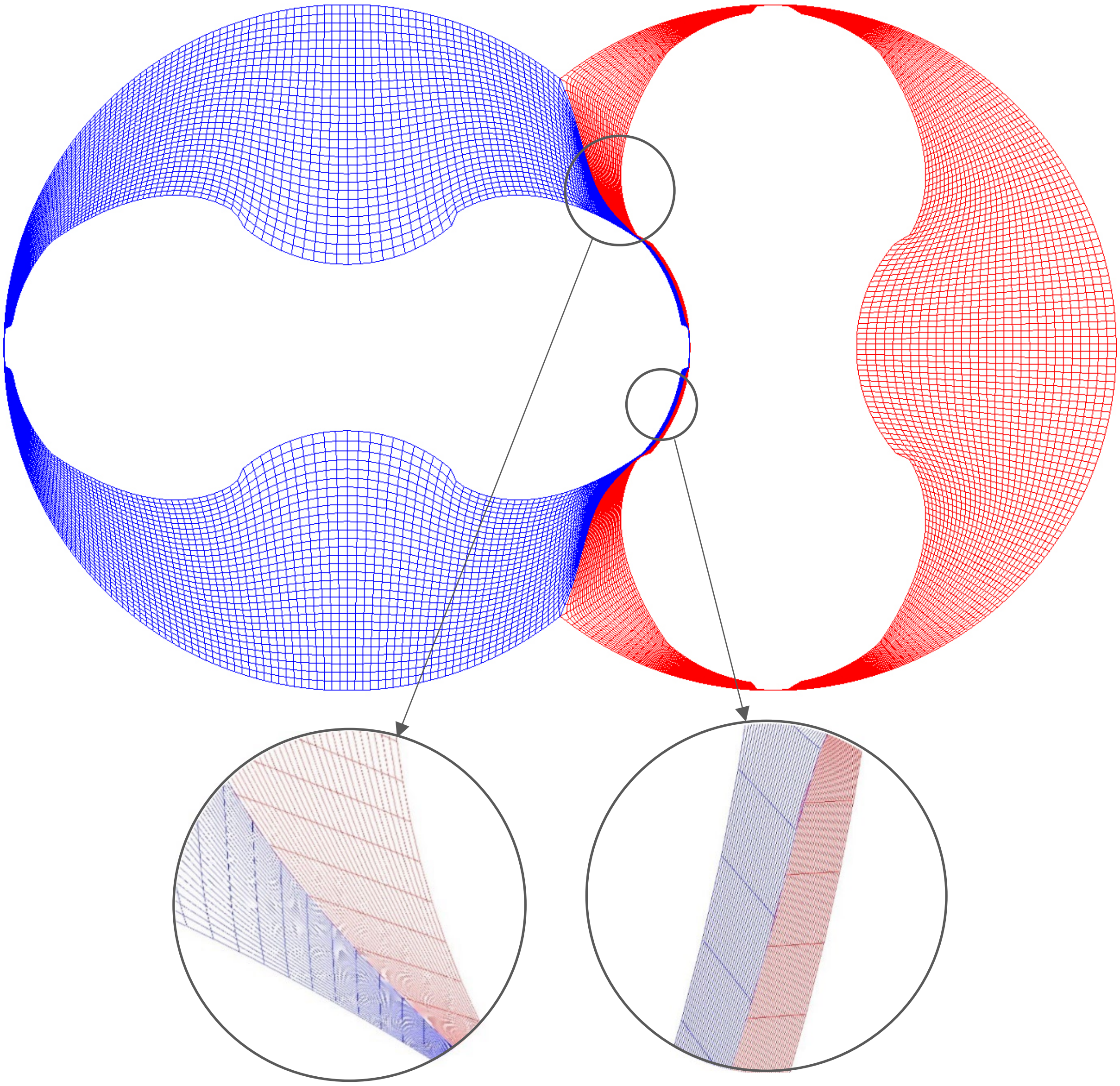

Figure 12 Non-conformal mesh generated in SCORG

The generated mesh consist of only hexahedral cells. From Figure 13 it can be seen that every node on one side of the interface can be matched with a node on the other side so there is no interpolation necessary. This makes the calculation more accurate and a lot faster. The presence of a non-conformal interface often causes convergence instability. To apply weighted interpolation and transfer the values Fluent creates an interior interpolation zone. Even though the node alignment along the mesh interface is not required, to prevent any issues with the creation of this zone, especially for dynamic meshes, poor cell alignment should be avoided.

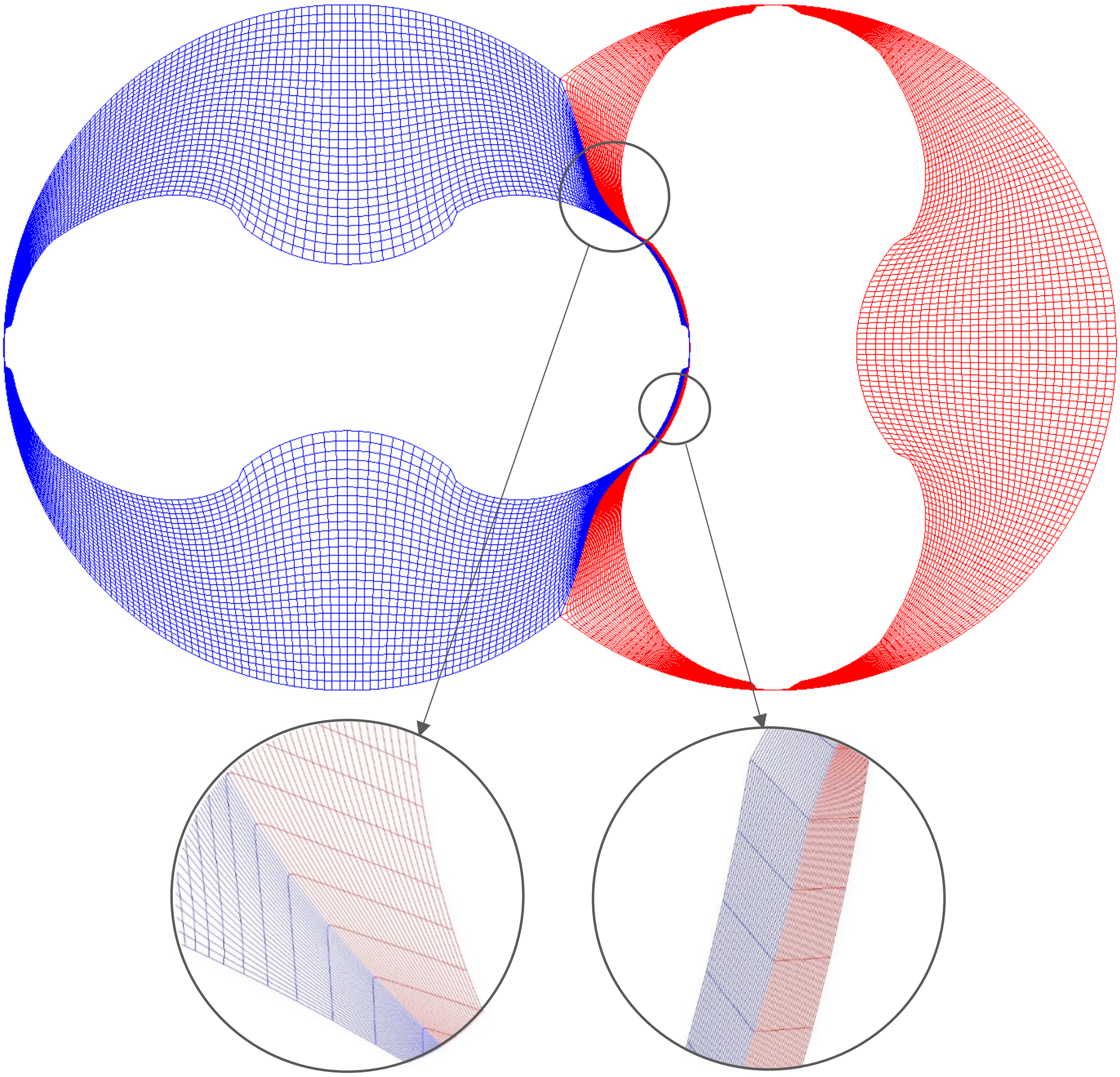

Figure 13 Conformal mesh generated in SCORG

4.1.2. Composite mesh

Figure 14 show the composite mesh which consists of five single domains:

- Inpipe domain (blue)
- Inport domain (teal)
- Rotor-fluid domain (yellow)
- Outport domain (orange)
- Outpipe domain (red)

- Axial clearance (purple)

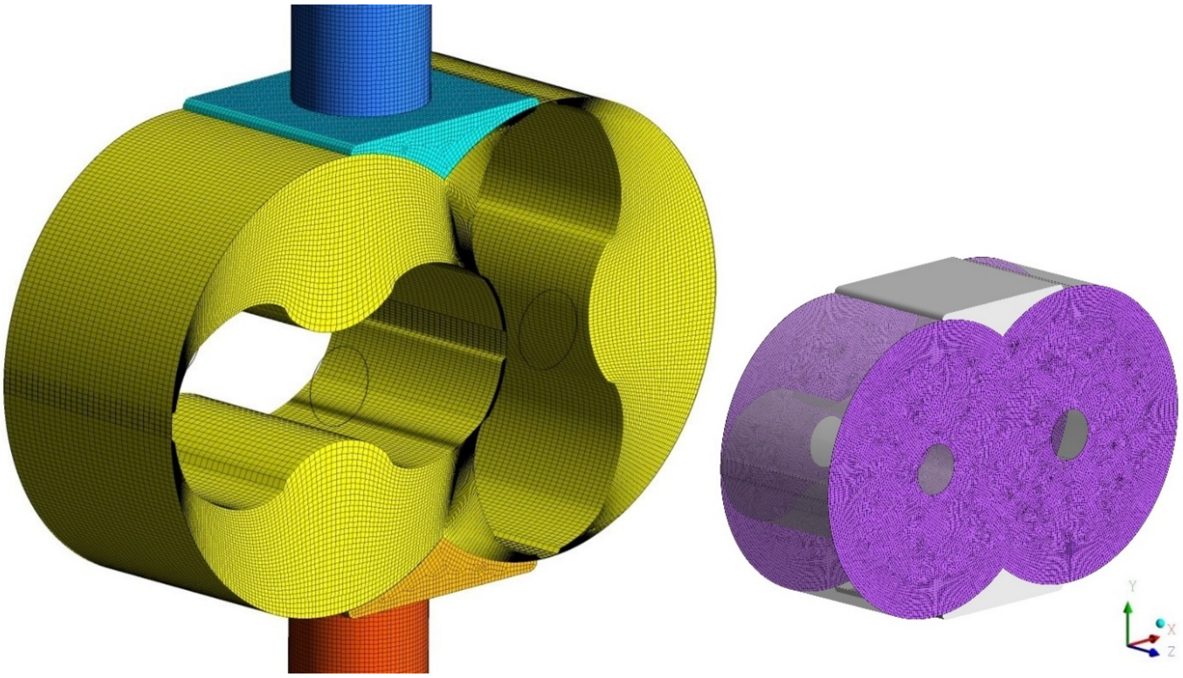

Figure 14 Non-conjugate CFD model computational domain

These five meshes are assembled non-conformally into a one composite mesh. There are 8 fluid-fluid non-conformal interfaces. In the non-conformal dynamic mesh there is an additional fluid-fluid non-conformal interface between the two dynamic domains. The computational domain consists of 1 366 176 control volumes in total.

Axial clearance domain in show in purple. This domain is scaled in z direction in CFX and then imported to Fluent. The trial-based evaluation process has been performed until the right axial gap, which aligns with the empirical data from tested operating conditions, was found. The mesh keeps the same topology while scaled as the number of control volumes stays the same.

4.2. Case setup and solver issues

4.2.1. Issues with non-conformal mesh

Initially the goal was to use non-conformal mesh because SCORG produces higher quality non-conformal meshes than conformal meshes due to stepped profiles. This is just the case for this specific geometry. To make the non-conformal mesh work in Fluent some compromises had to be made. The issue is with left-handed cells at interface zone connecting the two dynamic domains. To compute fluxes across the non-conformal boundary between two dynamic rotor domains in a non-conformal mesh, Fluent makes the interior zone where the two interface zones overlap. Due to poor alignment of cells at the interface, left-handed faces are generated in the newly made interior zone. Generally, left-handed faces occur mostly at locations where surfaces, which are non-conformally connected, have sharp corners. By continuing the simulation without correcting these cells the solver calculates the face normal wrongly which results in wrong flux calculation and divergence.

Failed attempts include:

- Turning off the dynamic mesh and running stationary case
- Incompressible fluid, energy equation turned off
- Reducing URFs
- Slowly increasing rotational speed
- Turning off secondary gradient on all cells
- Reducing accuracy by using first order (upwind) discretization schemes
- Imported interpolated converged solution from the model with deforming wall inside central pocket as an initial solution
- Using repair-face-handedness and repair-face-node-order commands in Fluent's TUI

The same non-conformal mesh was tested in ANSYS CFX solver and it works fine. CFX constructs control volumes around the nodes from element sectors and essentially makes a "new mesh" which doesn't have these issues.

The workaround for this issue in Fluent is to treat the interface patches as walls instead. The problem with this approach is that the velocity field in the central pocket will not be the same as in the real machine. As seen in Figure 15, the air temperature and pressure distribution looks reasonable with this interface absent, but it is seen that the velocity field in the central pocket is strongly influenced by the deforming wall which is placed inside the pocket.

Axial gap is uncalibrated so temperatures are lower due to higher mass flow rate. The gap specification si 70 in this simulation. The air exit temperature reaches 100 °C for 2000 rpm and 1.6 pressure ratio. The calculated mass flow rate is around 0,012 kg/s with 75% deviation from the measured value which is 0,007 kg/s. Later, the same simulation has been performed with the conformal mesh and an interface assigned between the two dynamic domains to evaluate the effect of this deforming wall inside the main pocket. The conformal mesh simulation for the same operating conditions achieved 0,0113 kg/s so the conclusion is that the wall impeeds the leakage flow, which is to be expected, but not too much. Therefore, the model presented in this section has shown satisfactory results.

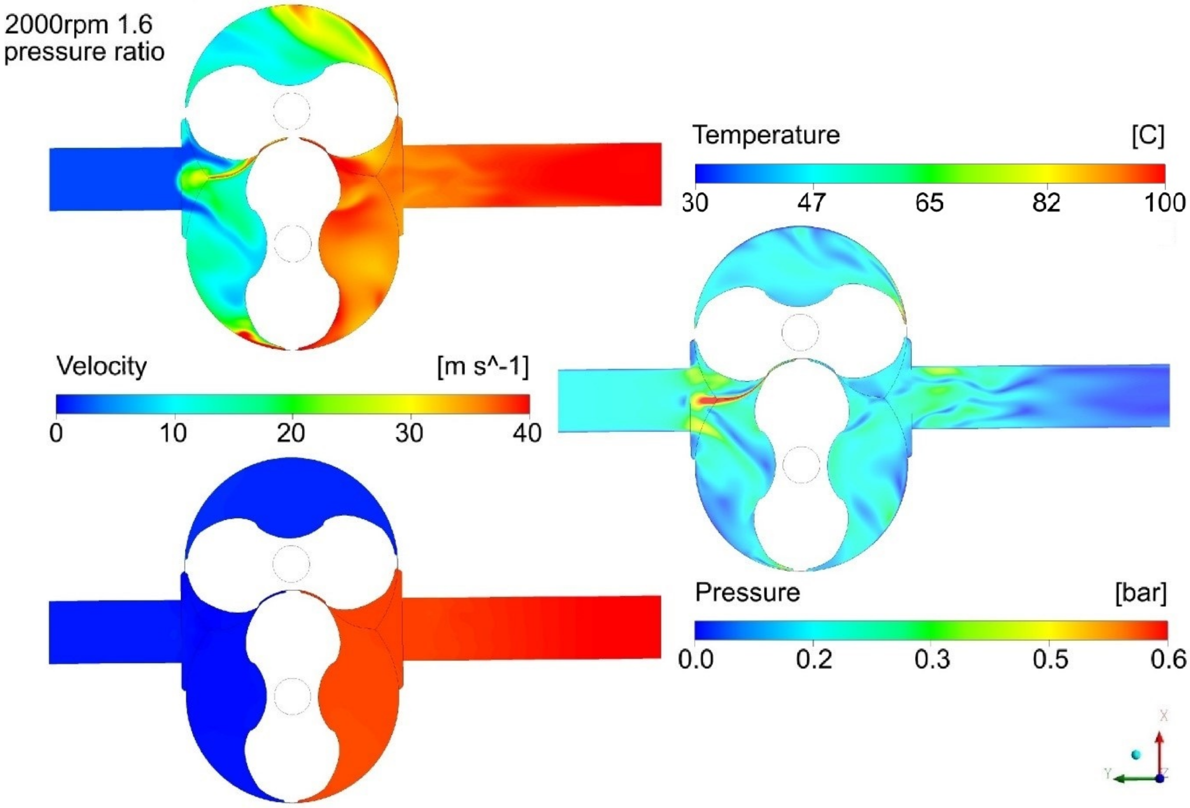

Figure 15 Numerical results from the model with non-conformal mesh

New conformal mesh was generated specifically to avoid this issue. This mesh will be lower quality than the non-conformal one due to stepped profiles, but the numerical model will be realistic. This will be followed by gap calibration and CHT simulation.

4.2.2. Boundary and initial conditions

To fully define the model the right boundary conditions and initial conditions need to be applied.

4.2.2.1. Inlet and outlet

CFD model will simulate the flow field under the operating conditions presented in Table 2. Both, inlet and outlet boundary conditions, are defined with pressure boundary condition according to the table below. The main difference in boundary conditions for different testing conditions is at the outlet which defines the static pressure value.

The turbulence intensity at the inlet was 5% and corresponding hydraulic diameter was assigned according to inpipe and outpipe diameter. The rest of boundary conditions are defined as stationary adiabatic walls with no-slip condition. This means there is no penetration of fluid or heat transfer happening across the boundary.

Table 2 Testing operating conditions

Pressure inlet [bar]	Temperature inlet [C]	Pressure outlet [bar]	Temperature outlet [C]	Mass flow rate [kg/s]
1.024	29.66	1.24	52.46	0.0033
1.024	29.19	1.232	59.06	0.0063
1.023	30.03	1.23	57.72	0.0092
1.023	30.92	1.439	82.31	0.0078
1.023	33.8	1.635	139.05	0.007

4.2.2.2. Additional rigid body motion UDF for rotor walls

DEFINE_GRID_MOTION only translates the mesh nodes with time, it doesn’t apply velocity on the wall boundary. Fluent’s standard boundary conditions can’t be applied for dynamic meshes controlled through the UDF. They are used for static meshes so another UDF function is needed.

The rigid body motion UDFs define the wall boundary condition for the male and female rotor walls. Both rotor walls are selected through the UDF code implemented as dynamic DEFINE_CG_MOTION macro. By using the predefined rotational speed this UDF assigns velocities to all the mesh nodes at the rotor wall for each time step. This value is directly assigned to the male rotor and for the female rotor, the value for rotational speed is multiplied by the gear ratio [26]. In this case the gear ratio is 1.0. This macro is executed during calculation, just like the DEFINE_GRID_MOTION macro.

4.2.2.3. Initialization

Fully converged numerical solution from the non-conformal simulation with deforming wall inside the main pocket was written to an interpolation file and imported to this simulation as an initial guess of the solution flow.

4.2.3. Simulation setup

For all the simulations performed with Fluent, air has been used as a working medium. Air is considered as a perfect gas which means that its density depends on temperature and pressure.

Table 3 Air properties

Items	Air specification
Density [$\boldsymbol{kg/m^3}$]	Ideal-gas
Specific heat [$\boldsymbol{J/(kgK)}$]	1006.43
Thermal conductivity [$\boldsymbol{W/(mK)}$]	0.0242
Viscosity	1.7894e-05

The simulation settings are shown in Table 3. The turbulence was modelled with the Shear Stress Transport (SST) k-ω model.

Table 4 Simulation settings

Items	Specification	Items	Specification
Solver	Pressure based	Spatial discretization	2nd order upwind
Turbulence model	k-ω SST	Turbulence numeric	1st order upwind
Working medium	Ideal air	Gradient	Least square cell based
Dynamic mesh method	Smoothing	Transient formulation	1st order implicit
P-V coupling scheme	Piso	Iterations/timestep	50

The flow was assumed to be subsonic below an overall pressure ratio of 1.9 and sonic above it [29]. Later, this assumption was confirmed to be correct by plotting the contours of Mach number in the domain of a case with highest rotational speed. Highest Mach number in the entire domain for 2000 rpm and 1.6 pressure ratio is 0.4 so the choice to go with pressure-based solver was correct.

4.2.4. Solver control

Underrelaxation factor defines how much of calculated value from the last iteration will be used in the next iteration. Transient compressible simulations demand very low Under Relaxation Factors so all URFs are set to 0.1. This significantly increases the stability of the simulation but at the expense of slowed down convergence. Convergence tolerance of 0.0001 is set to carry on the simulations.

4.3. Results and discussion

Roots blower geometry and meshing technique were presented in the previous sections. The challenges that emerged during simulation process were also presented and discussed. The numerical results for this case will be presented as following: In the first section the numerical results will be shown and in the second section the results will be compared against experimental data in order to validate the CFD model. Different physical phenomena that occur inside the compressor will be discussed as well.

4.3.1. Numerical results

Five cases have been investigated, each for different operating conditions:

1. 2000 rpm and 1.6 pressure ratio
2. 2000 rpm and 1.4 pressure ratio
3. 2000 rpm and 1.2 pressure ratio
4. 1500 rpm and 1.2 pressure ratio
5. 1000 rpm and 1.2 pressure ratio

The geometry is same for all these cases, the only difference is in the axial gap size which is calibrated for each testing condition separately.

Figures below show the postprocessed 3D numerical results from the first gap calibration simulation. When air gets displaced through a blower it gets compressed by the backflow and the leakage flow from clearance gaps transfer heat to the incoming air (Figure 16). As the cold low pressure incoming air gets heated by mixing with the leakage flow its volume increases, thus decreasing the volumetric efficiency.

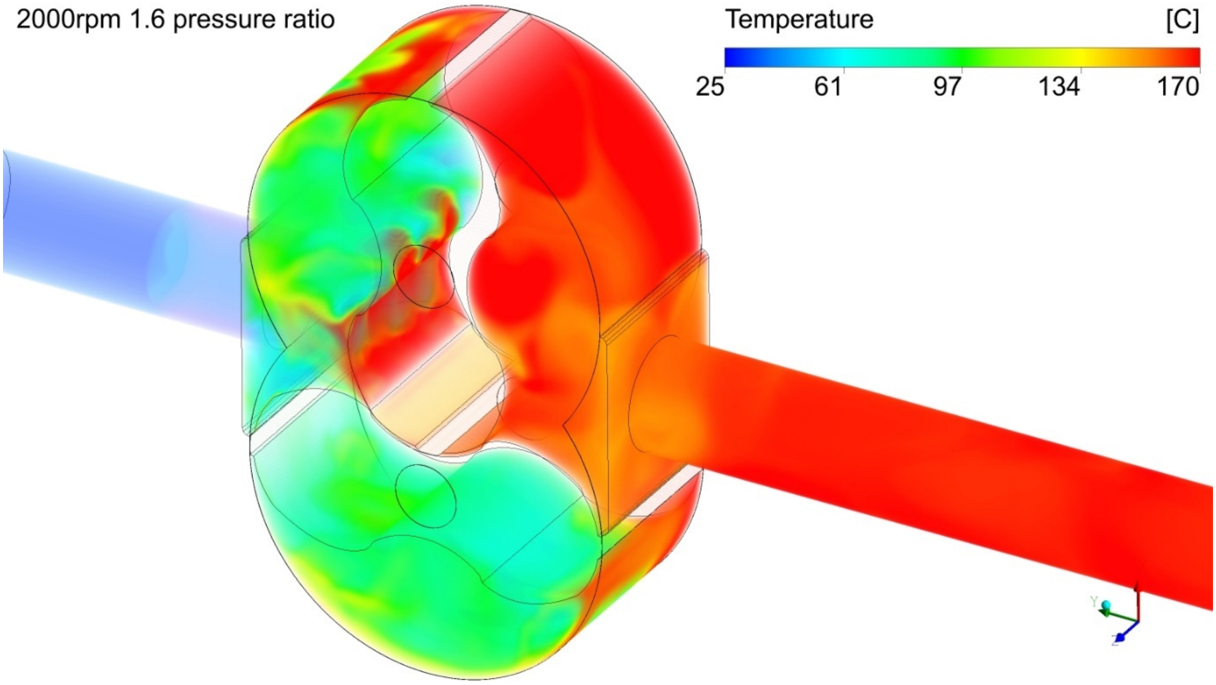

Figure 16 3D Temperature field for 2000rpm and 1.6 pressure ratio

Velocity field is presented in Figure 17. The leakage flow is clearly visible inside the interlobe clearance gap and the two tip clearance gaps. The leakage flow is accelerated inside the gaps where it achieves its maximum velocity.

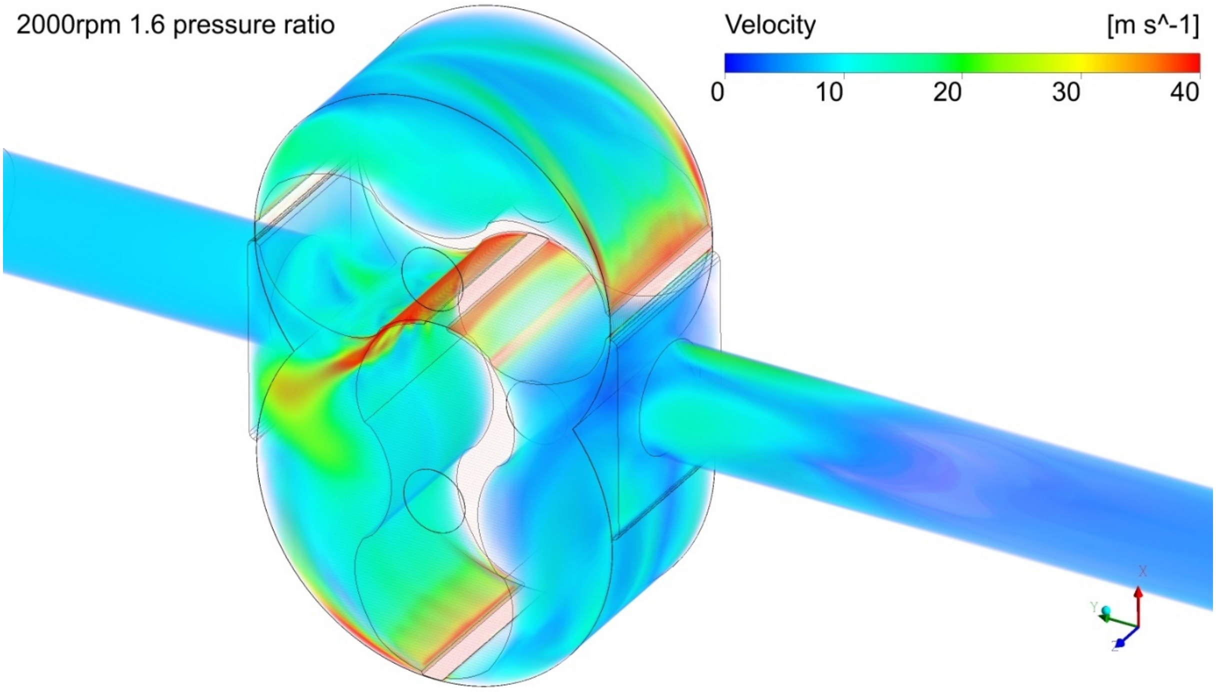

Figure 17 3D Velocity field for 2000rpm and 1.6 pressure ratio

Figures 18 and 19 show temperature field at the central plane for all five testing conditions. From the table 2 it can be seen that the gap calibration simulations over-predicted the exit temperature of air due to absence of heat transfer to rotors, casing and air surrounding the casing. The figures also clearly display the difference in the static temperature between different operating conditions for which the simulations were performed. The temperatures range from 71 to 165 °C. By increasing the pressure ratio, the temperature is also increasing significantly. The highest achieved exit gas temperature is 165 °C for the simulation with 2000 rpm and 1.635 pressure ratio. 1.635 pressure ratios is the highest pressure ratio tested. By going to even larger pressure ratios and higher rotational speed transonic flow can be expected inside the clearance gaps. This would require some modifications in the numerical model regarding the selection of the solver and additional mesh refinements in areas where shock wave is expected to occur. All the Figures present the numerical model with rigid body motion UDF attached to the male rotor wall boundary.

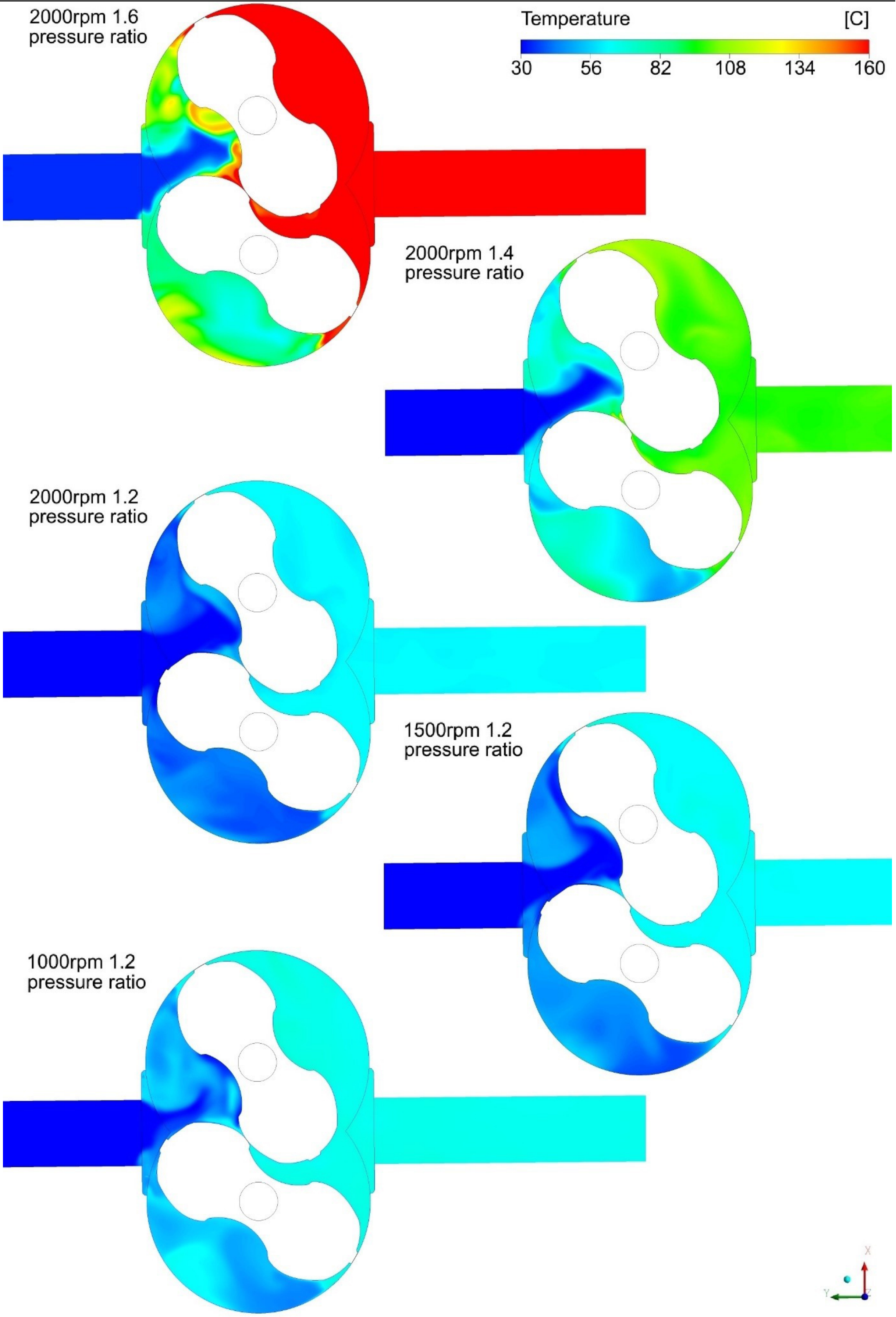

Figure 18 Temperature field at central plane at 2400 timestep

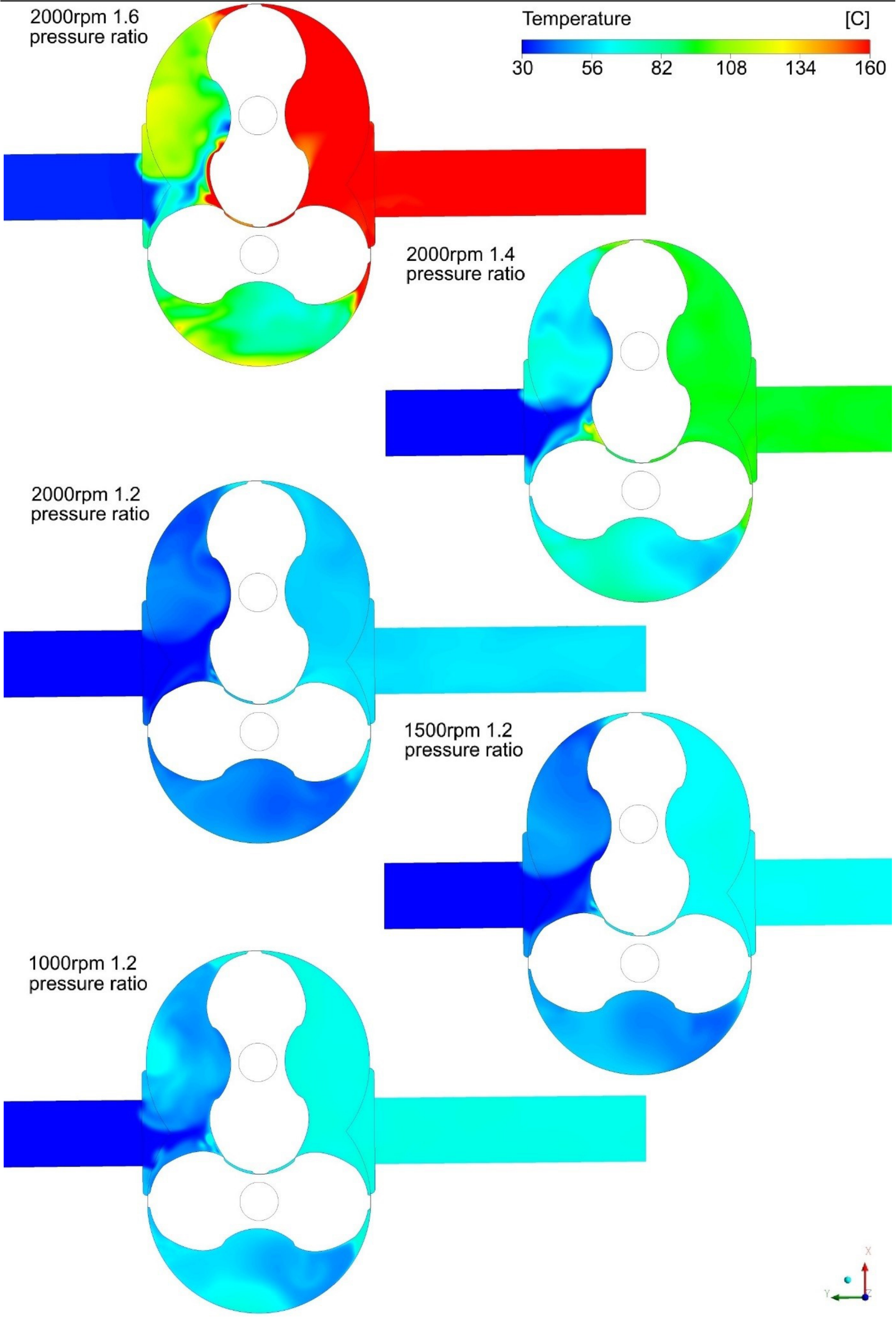

Figure 19 Temperature field at central plane at 2430 timestep

The following table shows the numerical results for each testing condition: This axial clearance gap value has been calculated using an trial-based procedure until the numerical solution for mass flow haven't fell below the acceptable threshold. Mass flow rate within +/- 10% was considered acceptable. If we compare the results for 2000 rpm and 1.6 pressure ratio with the results obtained with the non-conformal mesh model from chapter 4.2.1. which has a deforming wall inside the main pocket it can be observed that the achieved air exit temperature is much higher due to lower mass flow rate. The air exit temperature is 68% higher, while the achieved mass flow rate is 45% lower. These are significant differences between calibrated gap size of 150 and uncalibrated gap size of 70. Thus, it can be concluded that there is a large room for improvement with regards to volumetric efficiency by enhancing the desing of clearance gaps in rotary compressors.

Table 5 Numerical results from non-conjugate CFD analysis

Operating conditions	Mass flow rate [kg/s]	Exit temperature [°C]	Axial gap size [um]
1000 rpm 1.2 pressure ratio	0.00305	69	185
1500 rpm 1.2 pressure ratio	0.00614	67	224
2000 rpm 1.2 pressure ratio	0.00947	66	250
2000 rpm 1.4 pressure ratio	0.00778	105	190
2000 rpm 1.6 pressure ratio	0.00665	168	143

Axial gap ranges from 250 to 143. The design axial clearance gap in the machine is 150. These values are total values. As there are two gaps (one at each side of the rotor), the size of each is half the total value presented in the table. The smallest gap is calculated for the highest pressure ratio. For the same rotational velocity and higher pressure ratios, the calibrated gap size are smaller due to larger thermal deformations which cause shrinking of the clearance gap. When the pressure ratio increases, the mass flow rate decreases. The leakage cross sectional area is smaller and the leakage flow velocities are higher. This can be observed from the velocity fields in Figure 21. The rotor tip can be reshaped to increase pressure losses and reduce the leakage flow through the interlobe and the tip clearance gap.

Figure 20 displays pressure field at the central plane of a compressor. The absolute pressure of air at the inlet is set to 1 bar.

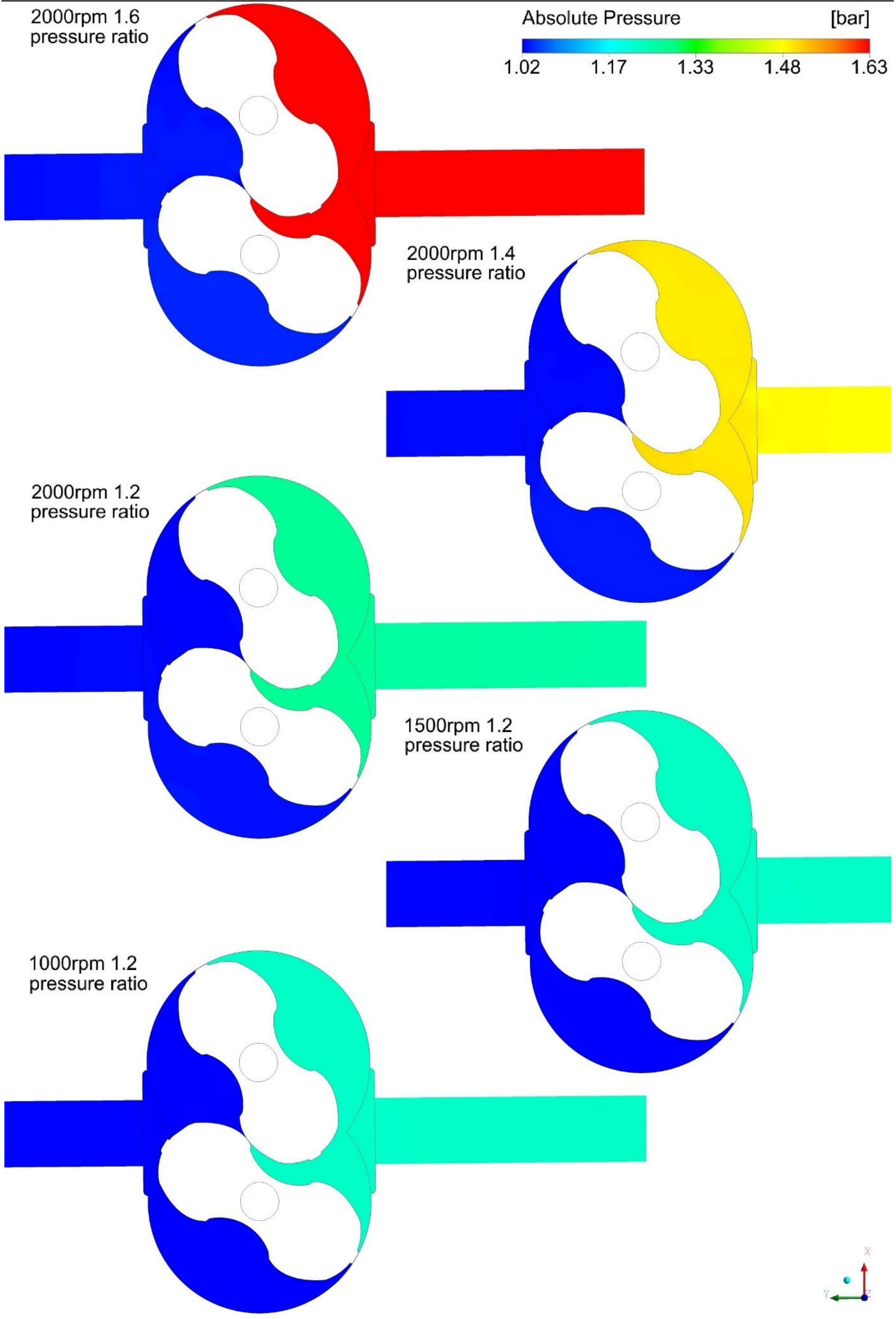

Figure 20 Pressure field at central plane at 2400 timestep

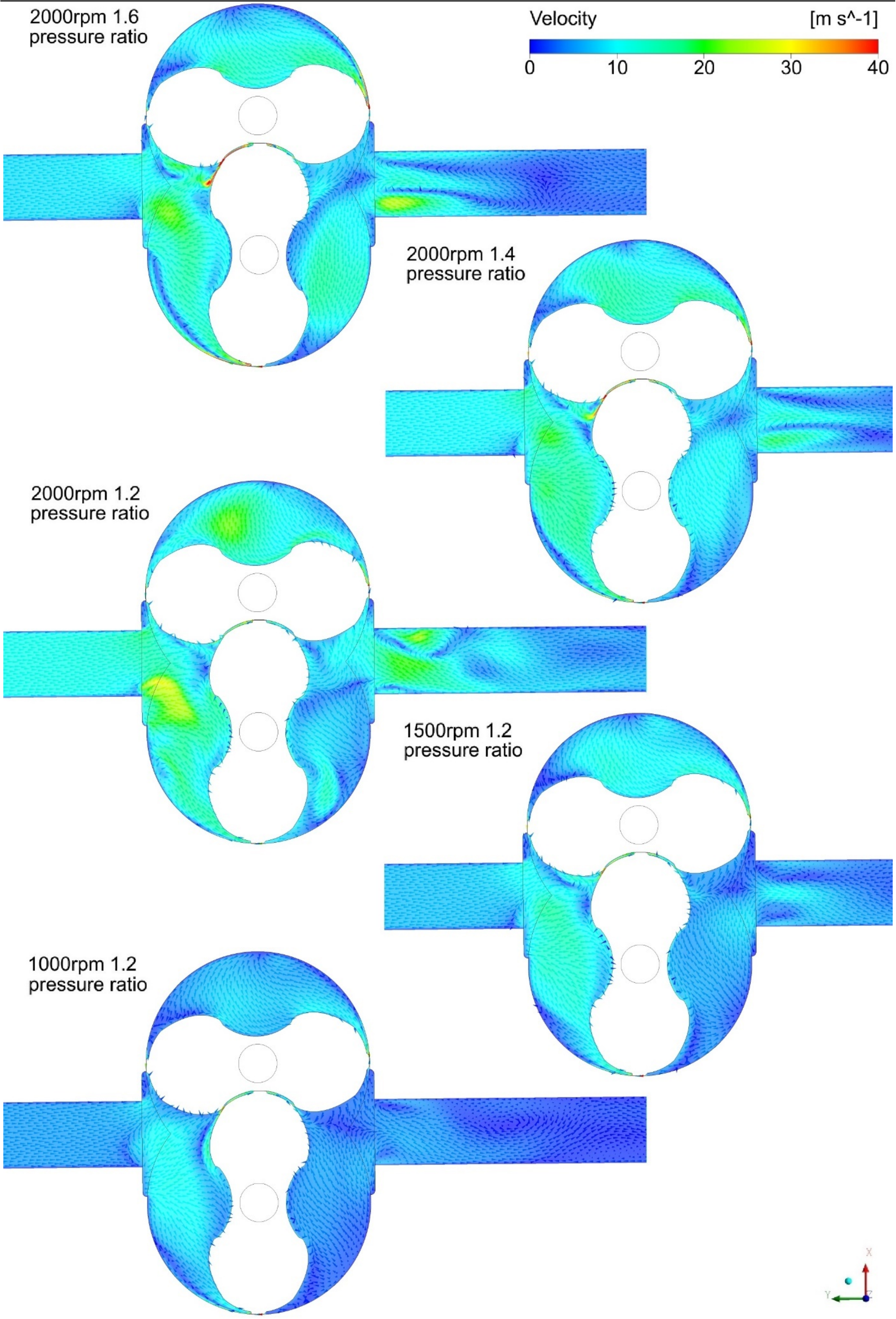

Figure 21 Velocity field at central plane at 2160 timestep

4.3.2. Validation

The CFD models in Positive Displacement Machines are usually validated by measuring integral parameters such as the total mass flow rate and power [20]. In the observed Roots blower flow and power validation have been achieved in all the observed cases.

Results in the tables below are presented for 2 different models for each tested rotational speed and pressure ratio (PR):

- Numerical model with attached rigid body UDF
- Numerical model without rigid body UDF

Table 6 Flow data from the model without rigid body UDF

	Mass flow rate [kg/s]	Flow %	Torque M [Nm]	Torque F [Nm]	Torque [Nm]	Power [kW]	Power %
1000rpm 1.2 PR	0.00305	-7.53	0.78	0.78	1.56	0.16	-1.40
1500rpm 1.2 PR	0.00614	-2.59	0.79	0.79	1.58	0.25	2.81
2000rpm 1.2 PR	0.00947	2.97	0.81	0.81	1.62	0.34	4.27
2000rpm 1.4 PR	0.00778	-0.25	1.57	1.57	3.14	0.66	1.78
2000rpm 1.6 PR	0.00665	-5.04	2.28	2.29	4.57	0.96	0.72

Table 7 Flow data from the model with rigid body UDF

	Mass flow rate [kg/s]	Flow %	Torque M [Nm]	Torque F [Nm]	Torque [Nm]	Power [kW]	Power %
1000rpm 1.2 PR	0.00352	6.56	-0.78	0.78	1.56	0.16	-1.40
1500rpm 1.2 PR	0.00665	5.58	-0.79	0.79	1.58	0.25	2.98
2000rpm 1.2 PR	0.01005	9.22	-0.82	0.81	1.63	0.34	5.13
2000rpm 1.4 PR	0.00830	6.41	-1.57	1.59	3.16	0.66	2.35
2000rpm 1.6 PR	0.00708	1.14	-2.33	2.28	4.61	0.97	1.61

The numerical model without rigid body UDF means that the rotor velocity is incorrect. From Table 4 and 5 it can be observed that the difference between the two models is not significant for the Torque integral value. However, it is also clearly visible that the mass flow rate increased for all five conditions. This increase in mass flow rates is direct consequence of assigning correct velocity values at the cells located on the rotor wall. The power presented in the table is effective power. There is also a noticeable difference between the male and female rotors. This is due to implementation of female rigid body UDF. The issue with this boundary is that the solver internally switches to local valve axis when applying In-Cylinder option in dynamic mesh. This makes implementation of the female rigid body UDF difficult because there is no simple way to assign the correct axis of rotation. Rigid body User Defined Functions are explained in chapter 3.4.2.

Both simulations show that the numerical model is able to provide adequate results. The largest deviation from the mass flow rate experimental result is 9.2 % for the model with rigid body UDF and 7.5% for the model without the UDF. Power validation has also been achieved with the largest deviation of 5.3%.

5. CONJUGATE HEAT TRANSFER ANALYSIS

This chapter discusses the method and results obtained with the CHT simulation. Heat transfer to solid domains of rotors and casing is included. First, the computational domain and case setup are presented. Then the numerical solution is discussed and compared against empirical data provided by City University London. The test Roots blower which will be used to obtain empirical data is modified to include transparent sapphire glas. By making the blower optically accessible, infrared thermography technique can be employed to obtain temperature fields on the surfaces of rotors and casing.

The main elements of the model are shown in Figure 21. The blower consist of the steel parts such as rotors and housing and the sapphire glass part which provides visual access for infrared thermography. The properties of these material are given in subchapter 5.2.2.

The computational mesh is made of 2 648 939 control volumes in total:

- 1 366 176 hexahedral and tetrahedral CVs in the solid domain
- 1 282 763 hexahedral CVs in the fluid domain

The geometry containing calibrated axial clearance domain and other fluid domains stayed the same. It was just upgraded with the solid elements and connected by non-conformal interfaces. The computational domain consists of multiple subdomains connected by non-conformal boundaries in which the node locations at the boundaries are not identical. This means that the mesh on connecting patches is not the same for different subdomains which leads errors in weighted interpolation which is used.

These interfaces are shown in Figure 21 together with the main elements of the CHT model. In total, there are 19 non-conformal interfaces:

- 8 fluid-fluid non-conformal interfaces
- 7 fluid-solid non-conformal interfaces
- 4 solid-solid non-conformal interfaces
- 1 fluid-fluid conformal interface between two dynamic rotor domains

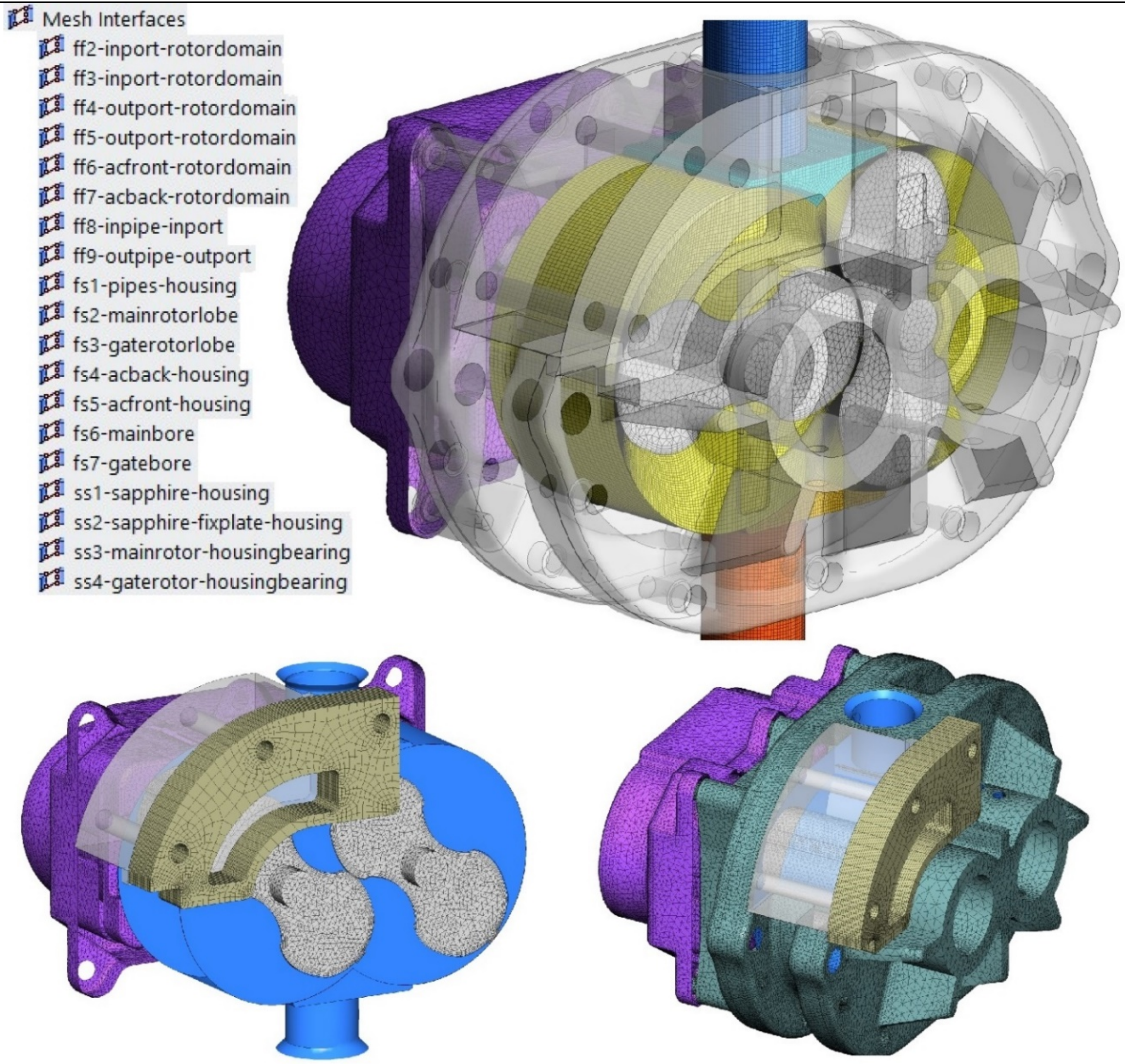

Figure 22 CHT Computational domain

All fluid-solid and solid-solid interfaces have been made using the mapped coupled wall option. The mapped mesh interface option is an alternative approach for modelling CHT between fluid-solid zones. It is more robust than the standard non-conformal interface formulations in cases where the interface zones are poorly aligned and penetrate each other or have gaps between them. Local tolerance is set to 10.

In the two solid rotor domains there is no need to control the motion of each node independently, so both rotors are specified as dynamic zones with mesh motion option. This allows Fluent to update the node positions by applying the solid-body motion equation so no relative motion between the nodes on the dynamic zone.

5.1. Case setup

All CHT simulations employed the same simulation setup as presented in chapter 4.2.3. except for a few additions which will be discussed in the following sections.

5.1.1. Boundary and initial conditions

5.1.1.1. Inlet and outlet

Inlet and outlet boundary conditions stayed the same as in the non-conjugate simulation and can be found in chapter 4.2.2.1. presented in Table 2.. The main difference in boundary condition specification is in the definition of wall type boundaries which are not adiabatic anymore.

5.1.1.2. Thermal boundary conditions

The boundaries which define the Roots blower geometry are defined as wall type boundary conditions. These walls are assigned one of the three types of boundary conditions discussed in chapter 2.3.3.

Coupled thermal boundary condition is used at the fluid-solid and solid-solid interfaces to capture thermal interactions between these zones by enforcing continuous temperature and thermal flux. This allows for obtaining the temperature field in both zones which are divided by the thermal interface. This can be achieved in just one CHT simulation. Equations which are solved in the solid and fluid domain are discussed in chapter 2.3. The coupled boundary conditions is the main pillar of Conjugate Heat Transfer analysis.

Outer wall which are in the direct contact with the surroundings are defined in two ways:

- As adiabatic or second kind boundary condition
- As convection or third kind boundary condition

First, the simulation is performed with the adiabatic thermal boundary condition assigned to the outer walls of the compressor due to lack of experimental data. Unfortunately, the results couldn’t be validated using this approach so there was a need to assign the convection thermal boundary condition at the outer boundaries. The latter approach has showed better alignment with empirical data.

5.1.1.3. Initialization

The flow field is not expected to change significantly with the inclusion of heat transfer so the numerical solution from adiabatic CFD simulations was used. Fully converged solution from the non-conjugate CFD simulation is written for each case to an interpolation file and then imported to CHT case as an initial guess of the solution flow.

5.1.2. Material properties

The existing CFD model with air as the working medium was extended with solid material properties provided form ANSYS Fluent material database. The following material properties of steel and sapphire glass were provided to the CHT model.

Table 8 Material properties of glass and steel [28]

Items	Glass specification	Steel specification
Density [$\boldsymbol{kg/m^3}$]	2401.7	8030
Specific heat [$\boldsymbol{J/(kgK)}$]	869.99	502.48
Thermal conductivity [$\boldsymbol{W/(mK)}$]	2.548	16.27

5.1.3. Time step control

As already discussed in chapter 3.2., conduction and convection processes are very different phenomena with each having its own rate of heat transfer. This posses a problem because in the case of conjugate heat transfer conduction represents a bottleneck in reaching quasi-steady state. Time marching in solid domain has to be accelerated to overcome this issue and allow for reaching quasi-steady state in reasonable amount of time. Fluid provides the option to specify solid time step size which enables a different time step size to be defined for solid domain. This way we will get closer to the run time of the real process.

For fluid domain the time step is determined from the pre-defined rotational speed and crank angle step size parameter. These are set inside in-cylinder options in dynamic mesh. The combination of these two parameters returns the time step size for in seconds. Essentially, two cases with different rotational speed will return different time steps if crank angle step size remains the same. This time step is very small and it will be maintained in fluid domain.

The ratio between the fluid and solid domain time steps can be defined as the time-scale factor tsf:

$$tsf = \frac{\Delta t_s}{\Delta t_f} \tag{5.1}$$

Table 9 shows time-scale factors which will be applied for each operating condition. The time-scale factors are chosen to achieve the same run time for all operating conditions so solid zone time step size is the same.

Table 9 Flow data from the model without rigid body UDF

	1000 rpm 1.2 PR	1500 rpm 1.2 PR	2000 rpm 1.2 PR	2000 rpm 1.4 PR	2000 rpm 1.6 PR
Crank shaft speed [rpm]	1000	1500	2000	2000	2000
Crank angle step size [°]	1	1	1	1	1
Fluid zone time step [s]	0.000166	0.000111	8.33e-5	8.33e-5	8.33e-5
Solid zone time step [s]	0.833	0.833	0.833	0.833	0.833
Time-scale factor	5000	7500	10000	10000	10000

5.2. Results and discussion

In the previous sections, all input data needed for CHT simulations were presented. In this section, the impact of heat transfer inclusion is analysed and numerical results are presented for measured operating conditions. In total, five different operating conditions were simulated and the results are validated. City University London provided high quality experimental reference data set for validation of the numerical model established in this thesis. The test performance parameters were measured on a test compressor in a laboratory at City.

5.2.1. Numerical solution

5.2.1.1. Time-scale factor analysis

The simulation was performed at 2000 rpm and 1.6 pressure ratio for 7200 timesteps while defining outer walls as adiabatic. The objective is to heat up solid elements until the air exit temperature achieves its experimentally measured value and after this value is reached try to validate the lobe surface temperatures. The time-scale factor analysis was performed to determine which time-scale factor suits best this CHT simulation.

The graph in Figure 21 shows that when the simulation starts the exit temperature of air starts decreasing due to heat absorption from cold solid elements because the solid domain was initialized to ambient temperature. From there it starts to rise gradually until it reaches quasi-steady state. It can be observed that the time-scale factor of 10000 can achieve the measured exit gas temperature of 412 °C, while the time-scale factor of 5000 reaches around 400 °C. At 6480th Timestep the spatial discretization accuracy has been increased to 2nd order which resulted in the observed spike after the continued gradual rise of the air exit temperature.

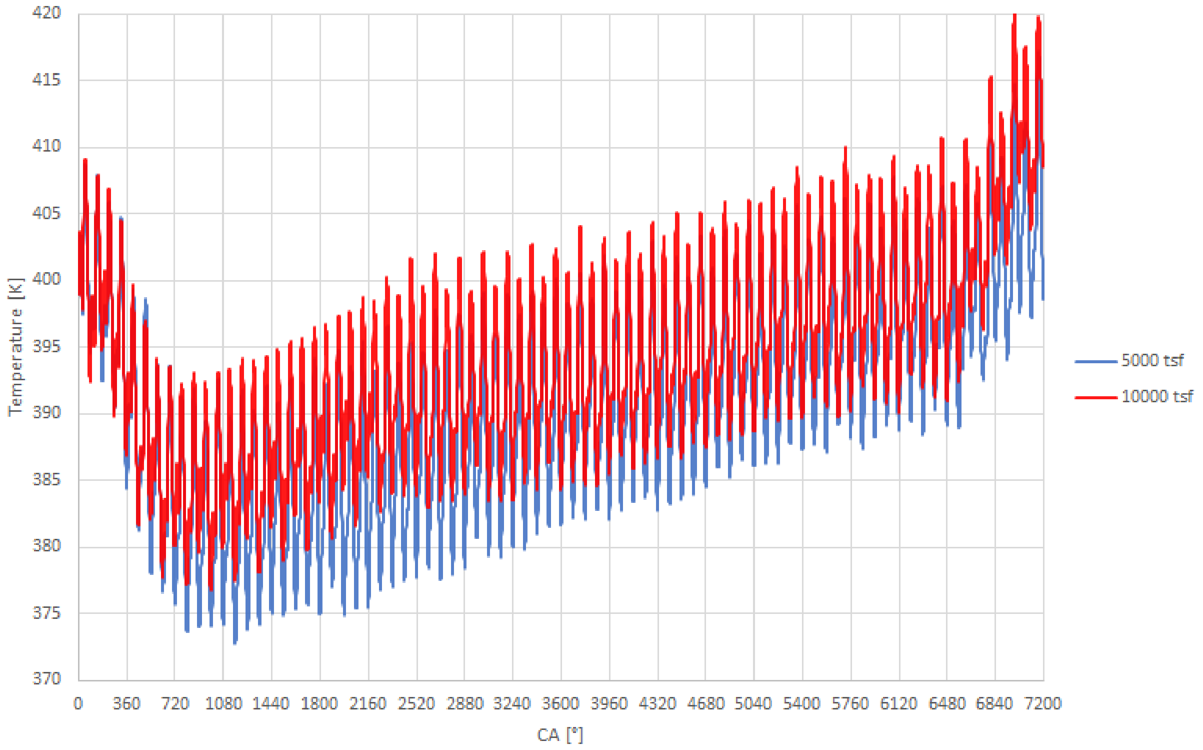

Figure 23 Exit temperature of air for 5000 tsf and 10000 tsf

Figure 22 displays the mass flow rate graph for 10000 tsf. The average measured flow rate of 0.007 kg/s has been achieved after the spatial discretization accuracy has been increased to 2nd order at 6480th timestep.

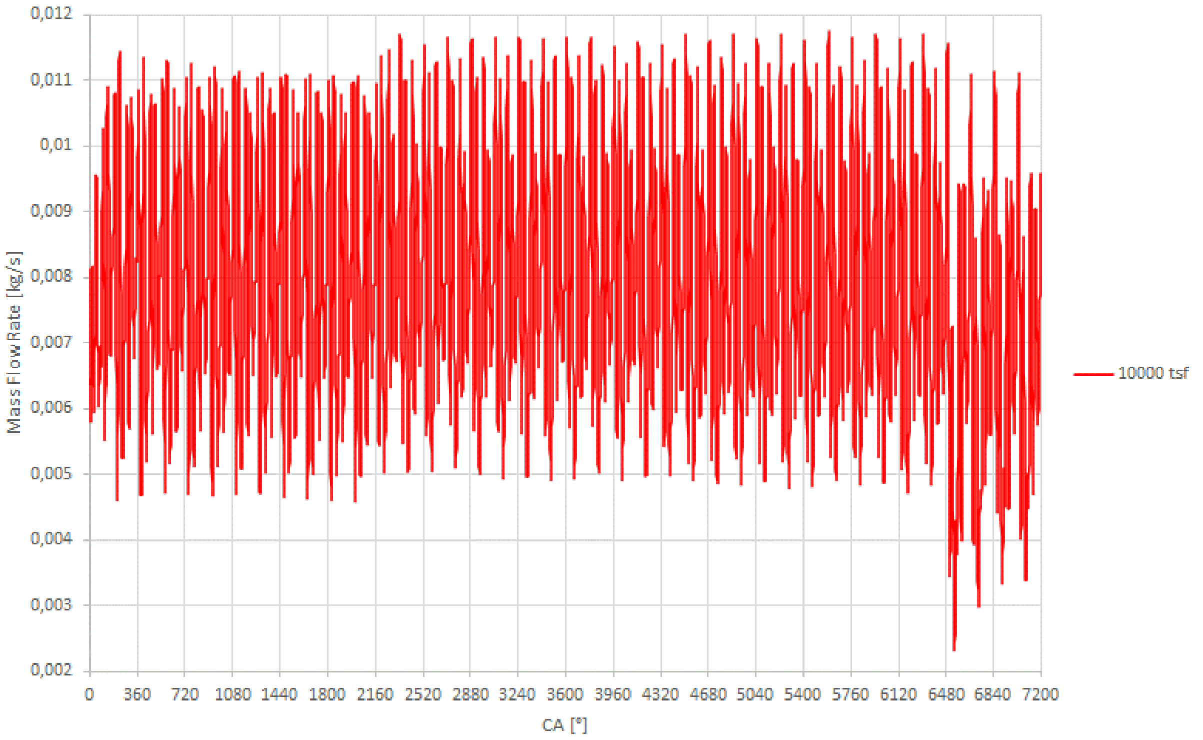

Figure 24 Mass flow rate for 10000 tsf

Unfortunately, for time-scale factor of 10000 the lobe surface temperatures were significantly lower than what was measured by infrared thermography. Even though it has provided correct air exit temperature, this process is very time consuming and didn't provide data reliable enough to continue its research for different operating conditions.

5.2.1.2. Simulations with convective boundary condition

Due to the high computational time required for time-scale factor analysis, the approach with adiabatic thermal boundary condition has been abandoned though it has the ability to accurately predict the air exit temperature. From there, the numerical modelling progressed on to the inclusion of convective thermal boundary condition. Simulations were conducted for the same range of operating conditions as in the non-conjugate simulations.

The imposed convective boundary conditions on outer walls have the same parameters h and T_∞. h is the heat transfer coefficient and T_∞ is the temperature of air surrounding the casing. The heat transfer coefficient encountered in natural convection is very low due to low fluid velocity. The value of 10 $\mathrm{W/(m^2K)}$ was assigned to the outer walls to heat transfer coefficient, as recommended in literature.

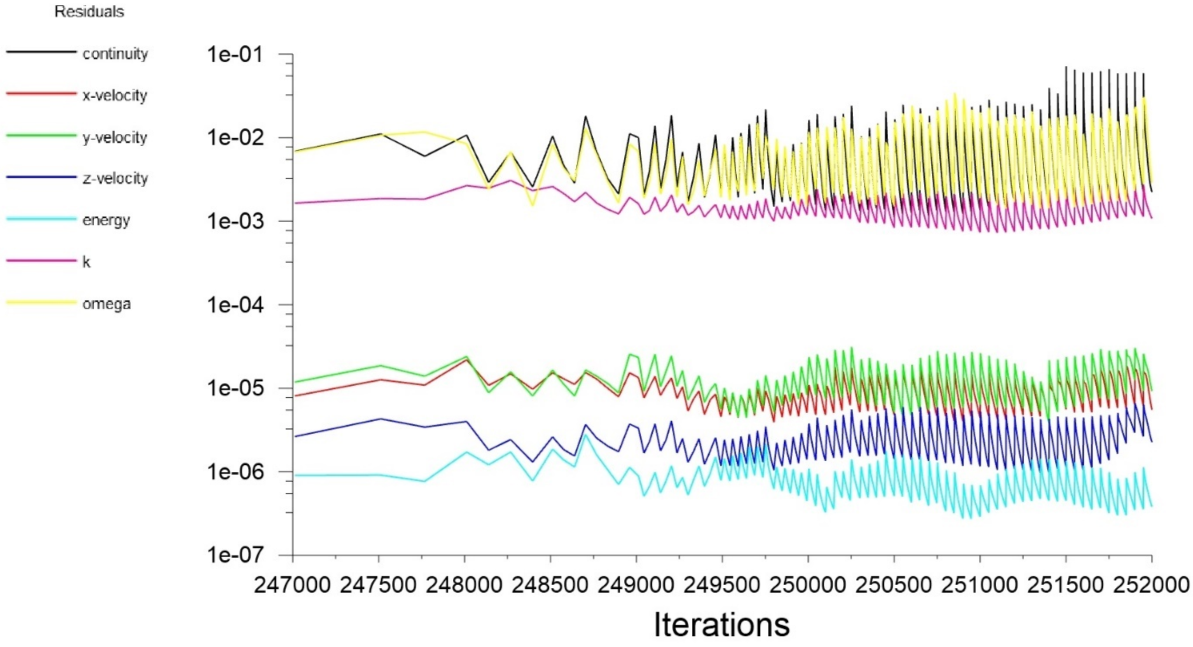

Figure 25 Residuals for monitoring convergance

For all the simulations, iterations were performed until residuals dropped to an acceptable level of 10e-3. Figre 25 shows the residuals for a CHT simulation for 2000 rpm and 1.6 PR. In Table 10 numerical results are given for each operating condition. Simulation is performed for 5040 timesteps with accumulated timestep presented in the table for each domain. Conduction in solid domain is accelerated by using time-scale factor to achieve compressor run time of 70 minutes. It can be noted that the flow validation has been preserved. Mass flow rate for each operating point match the measurement results (Table 2) well. The highest achieved mass flow rate is 0.0098 kg/s, while the lowest is 0.0036 kg/s. Good correlation is also observed with the air exit temperatures.

Table 10 Numerical results from CHT analysis

	1000 rpm 1.2 PR	1500 rpm 1.2 PR	2000 rpm 1.2 PR	2000 rpm 1.4 PR	2000 rpm 1.6 PR
Solid initialization temperature [°C]	37	52	52	72	117
Solid-time [min]	70	70	70	70	70
Flow-time [s]	0.84	0.56	0.42	0.42	0.42
Exit temperature	51	58	57	84	143
Mass flow [kg/s]	0,0036	0.0066	0.0098	0.0083	0.00735

The following figures show the temperature field contours for each operating condition. From the contour map it can be seen that the achieved exit temperatures are slightly lower across the board, when comparing them to temperatures from the non-conjugate analysis (Figures 18 and 19). This is expected as heat transfer occur from the hot pressurized air to the rotors and casing. This heat eventually dissipates into the surrounding air. The highest achieved air exit temperature is 143 °C, while the lowest is 51 °C. This model has both rigid body UDF functions applied to the rotor walls, despite difficulties with assigning the correct axis of rotation for the female rotor. Several attempts have been made to achieve the same accuracy without female rigid body UDF, but without success. There is simply too big of a difference between the correctly assigned male rotor velocity and the female rotor velocity which is assiged by Fluent internally, using an unknown specification.

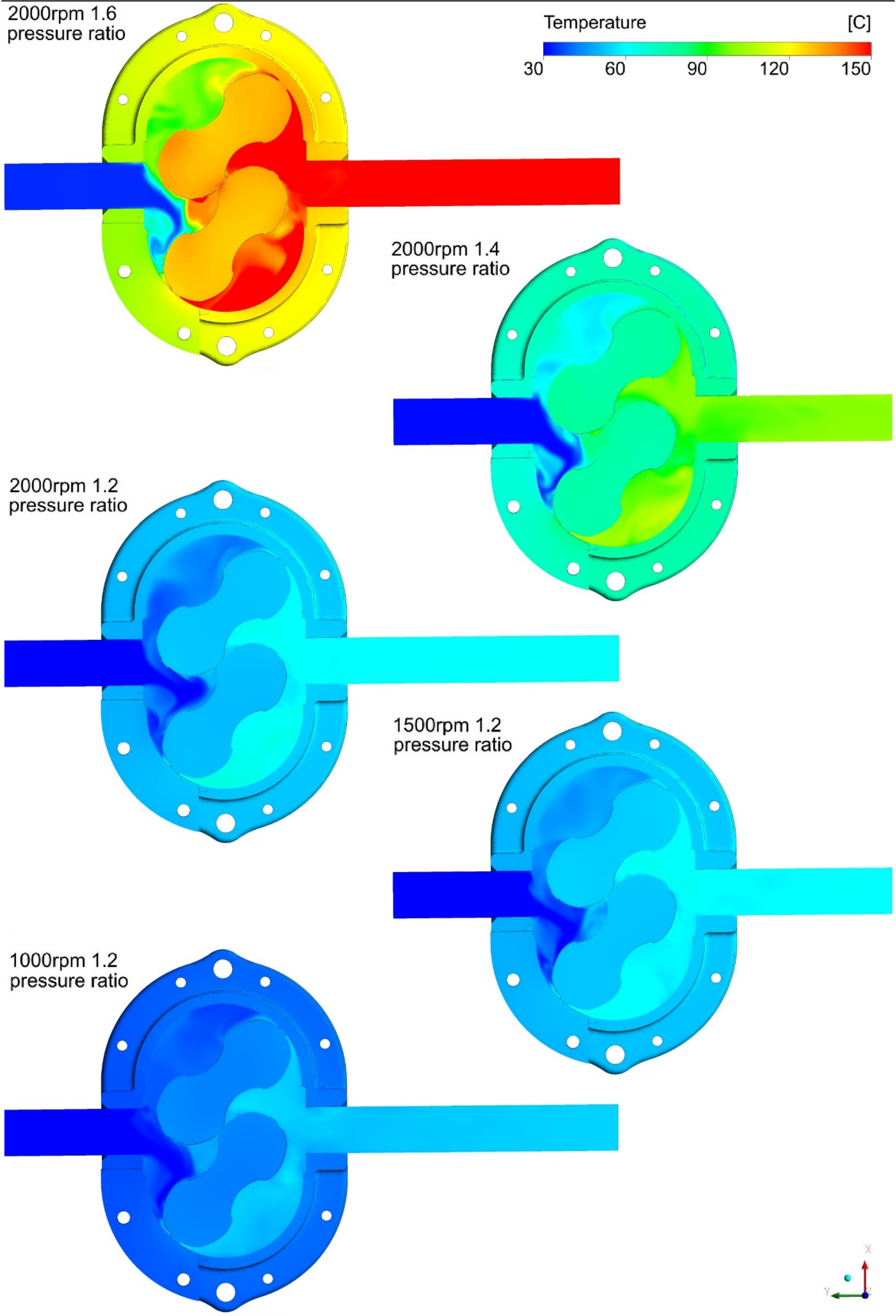

Figure 26 Temperature field for 2000 rpm and 1.4 PR

5.2.2. *Surface temperature validation*

By calibrating the leakage gap size, the flow and power validation has already been achieved in the non-conjugate CFD model. This validation has been kept throughout the conjugate heat transfer simulation for all operating conditions. The main objective in this chapter is to validate rotor surface temperatures. A qualitative comparison between the numerical results obtained by CHT simulation and provided experimental data will be made. The experimental data presented in thermograms in the Figures below shows an avereged temperature field at the surface of the male rotor for each testing condition. The experimental data were provided by City University of London.

Figures 26 and 27 show the lobe surface temperature for 1.6 and 1.4 pressure ratio. These are the highest pressure ratios so higher temperatures are expected. Comparison with thermograms show that the transient and strictly coupled CHT model was able to predict the results adequatly.

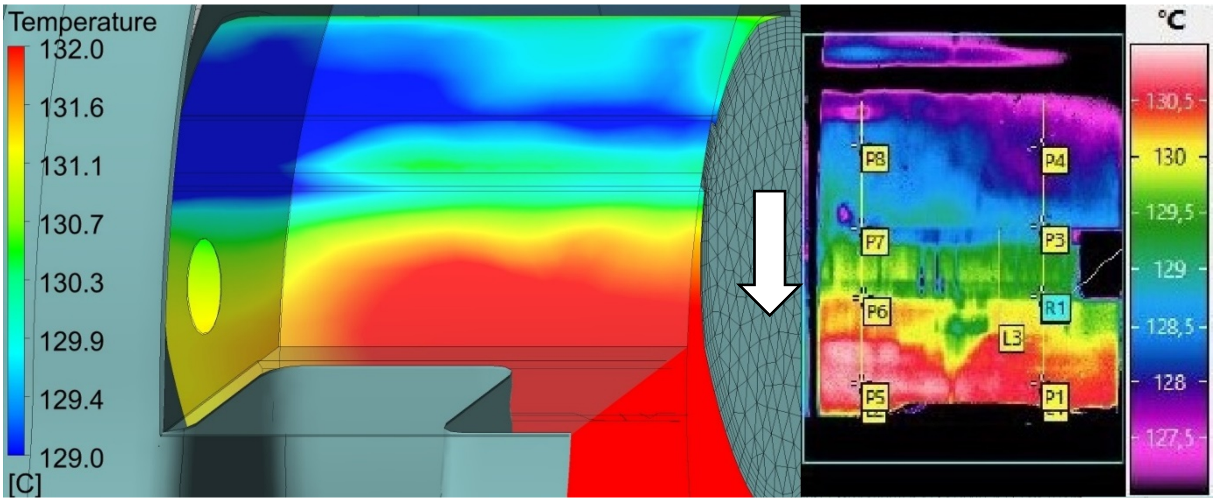

Figure 27 Lobe surface temperature for 2000 rpm and 1.6 PR

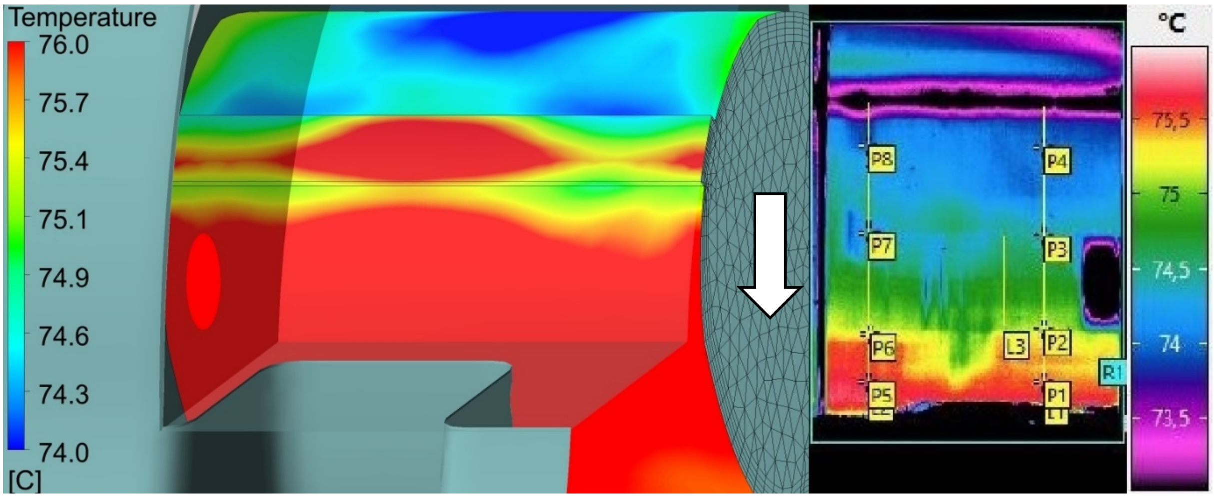

Figure 28 Lobe surface temperature for 2000 rpm and 1.4 PR

It can be observed that the temperature profile on the tip is slightly different. There is a clear increase in temperature in the middle of the tip which is caused by very intense leakage flow in this area for. There are also thermal traces from the axial gap leakage flow on the suction side. These are visible from the both sides of the lobe. Quantitative range of the surface temperatures are well aligned with the thermograms on the right side but there is a slight difference in the qualitative variation of temperature field.

The values obtained from the numerical simulations for other three operating conditions are mostly in good agreement with experimental data. However, there is a slight discrepancy between experimental and numerical data obtained for 1000 rpm and 1.2 pressure ratio. Lobe temperature is a bit lower than what was measured with infrared thermography. This deviation is around 10% with respect to the measured range.

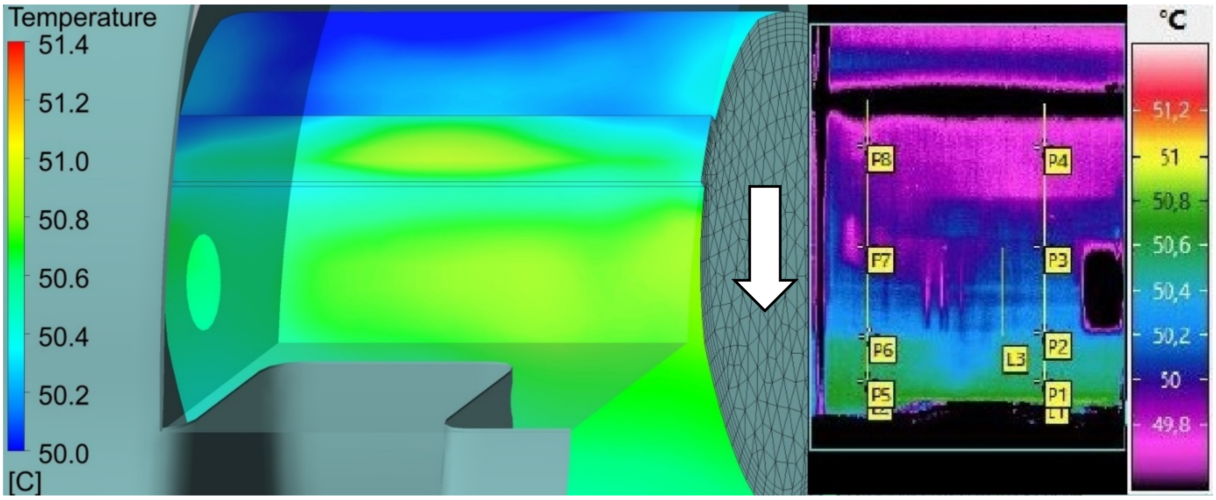

Figure 29 Lobe surface temperature for 2000 rpm and 1.2 PR

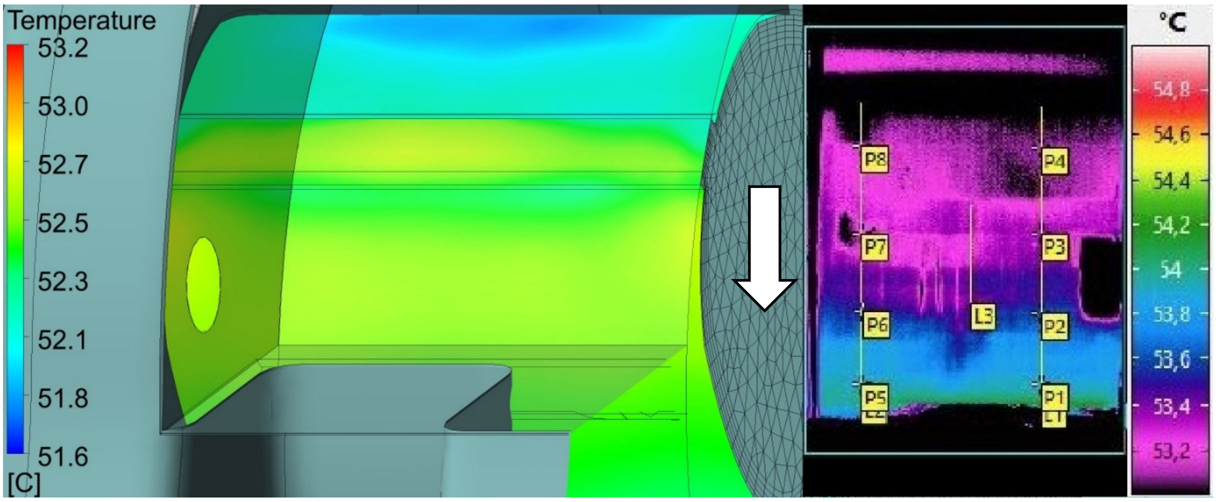

Figure 30 Lobe surface temperature for 1500 rpm and 1.2 PR

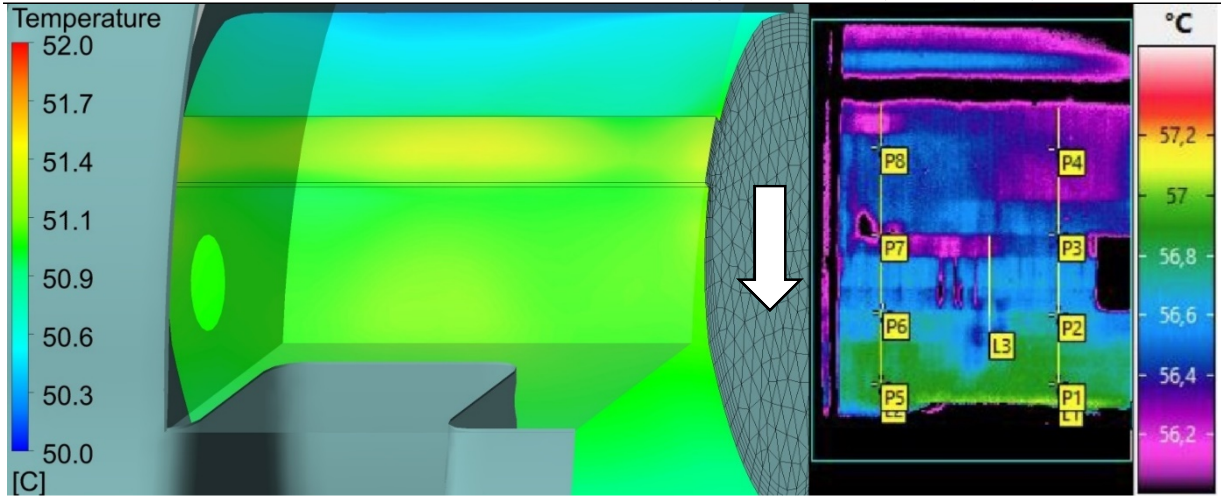

Figure 31 Lobe surface temperature for 1000 rpm and 1.2 PR

Figure 32 presents instantaneous temperature at outer surfaces of the compressor for the two highest pressure ratios 1.6 and 1.4. Outer surface temperatures obtained by numerical analysis are in good agreement with experimental measurements. There is a slight qualitative diference in temperature variation in the heat sink on the right side of the compressor but within acceptable devation.

2000rpm 1.6
pressure ratio

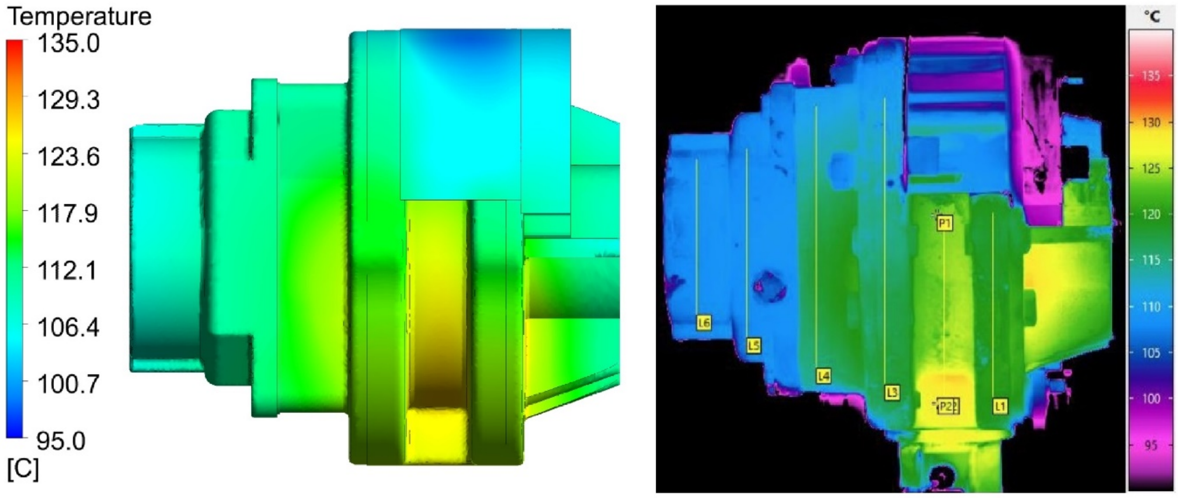

2000rpm 1.4
pressure ratio

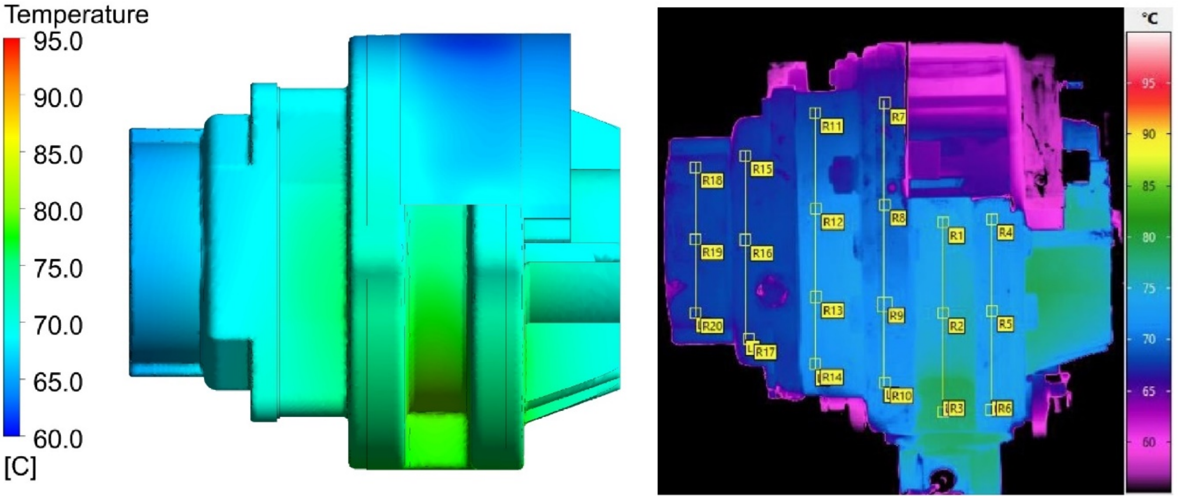

Figure 32 Temperature field contours of outer casing for 1.6 and 1.4 pressure ratio

6. CONCLUSION AND FUTURE WORK

In this Thesis Conjugate Heat Transfer numerical models are employed to analyse heat transfer from hot pressurized air to rotors, casing and surrounding air for the purpose of obtaining surface temperatures and comparing agains experimental data. Five cases have been investigated, each for different operating condition. Simulations were carried out using ANSYS Fluent which employs finite volume method. The geometry is the same for all these cases, the only difference is in the axial clearance gap size which is calibrated for each testing condition separately. The comparison with the gathered experimental data has shown that the numerical simulations produced satisfactory results. The simulations were able to capture the flow field adequately and provide temperature field of solid components.

Power and mass flow validation were achieved in every simulation. Axial gap ranges from 250 to 143. The design axial clearance gap in the machine is 150. The following trends have been established. If the the same rotational speed is maintained while increasing the pressure and consequently temperature, the axial gap should be decreased. And if the same pressure ratio is maintained while increasing the rotational speed, the axial gap should be increased. The small changes in size of the axial clearance gap has found to be very impactful on the mass flow rate and on the air exit temperatures. It has been observed that there are significant differences between calibrated clearance of 150 and uncalibrated clearance size of 70 for 2000 rpm and 1.6 operating point. This has confirmed the assumption that there is a large room for improvement with regards to volumetric efficiency by enhancing the desing of clearance gaps in Roots blowers. Non-conjugate CFD analyses over-predicted the exit temperature of air due to absence of heat transfer. The highest achieved air exit temperature is 165 °C.

The aproach by using adiabatic thermal boundary condition on the outter boundaries showed to be unrealistic and time consuming. The time scale factor of 10000 has been shown to align better with experimental data, while the time scale factor of 5000 underpredicted the exit temperature. Introducing convective heat transfer on the outer boundaries brought the numerical results closer to the experimental data obtained by infrared thermography. The air exit temperatures numerically calculated by this model have been successfully validated. The highest achieved air exit temperature is 143 °C in comparisson to 165 °C achieved by non-conjugate CFD analysis. The numerically obtained surface temperatures are also in good agreement with the experimental data sets regarding the quantitative temperature range. However, there are noticeable differences in qualitative temperature variations in some test cases. The largest deviation is found to be for 1000 rpm and 1.2 pressure ratio and is around

10% with respect to the measured range of lobe surface temperatures. In addition, it can be noted that the incorrect rotor velocity does not affect the integral parameters too much. However, it has a significant impact on the temperature profile at the rotor surface as the numerically obtained temperature results could't be validated without assigning the correct velocity field on rotor wall by rigid body UDF.

In further considerations, it is necessary to perform a mesh sensitivity analysis and investigate in more detail the influence of the heat transfer coefficient, assigned on the outter boundaries, on the temperature field in the rotor and compressor housing. Future work should expand on this CHT analysis by performing Fluid Structure Analysis on a Roots blower with the aim of calculating the deformations of solid components. By using system coupling for two way FSI, it could be possible to predict the deformations and help minimize the clearance gap. Furthermore, by using this knowledge the rotor tip can be redesigned with different shapes and features in order to reduce the leakage flow and improve efficiency.

REFERENCES

[1] R. Saidur, N. A. Rahim, and M. Hasanuzzaman, "A review on compressed-air energy use and Energy Savings," *Renewable and Sustainable Energy Reviews*, vol. 14, no. 4, pp. 1135–1153, 2010.

[2] M. A. Pellow, C. J. Emmott, C. J. Barnhart, and S. M. Benson, "Hydrogen or batteries for grid storage? A net energy analysis", *Energy & Environmental Science*, vol. 8, no. 7, pp. 1938–1952, 2015.

[3] Y. Zhang, Y. Zhao, and X. Peng, "Three-dimensional CFD Simulation of a Roots Blower for the Hydrogen Circulating Pump", *International. Compressor Engineering Conference*, p. 2625, 2018.

[4] *European Commission*, [Online]. Available: ec.europa.eu/eurostat/databrowser/view/nrg_pc_205/default/table. [Accessed: 15-Apr.-2022].

[5] S. Rane, "Grid Generation and CFD Analysis of Variable Geometry Screw Machines", PhD thesis, City University London, 2015.

[6] R. N. Brown, *Compressors: Selection and Sizing*, Houston: Elsevier, 2005.

[7] N. H. Thai and N. T. Trung, "Establishing Formulas for Design of Roots Pump Geometrical Parameters with Given Specific Flowrate", *Vietnam Journal of Science and Technology*, vol. 53, no. 4, p. 533, 2015.

[8] S. H. Sun, A. Kovacevic, C. Bruecker, A. Leto, G. Singh, and M. Ghavami, "Numerical and experimental analysis of transient flow in roots blower", *IOP Conference Series: Materials Science and Engineering*, vol. 425, p. 012024, 2018.

[9] D. W. Tryhorn, "Blower Noise and Solution: An Introduction to the A.W. Convel Blower", *International Compressor Engineering Conference*, p. 227, 1976.

[10] T. Gaimpaolo, *Compressor Handbook: Principles and Practice*, Georgia: The Fairmont Press, 1939.

[11] N. S. Mian, S. Fletcher, A. P. Longstaff and A. Myers, "Towards obtaining robust boundary condition parameters to aid accuracy in FEA thermal error predictions", *2nd Annual EPSRC Manufacturing the Future Conference*, 2013.

[12] S. Rane and A. Kovačević, "Algebraic generation of single domain computational grid for twin screw machines Part I – Implementation", *Advances in Engineering Software*, vol. 107, pp. 38–50, 2017.

[13] S. Rane and A. Kovačević, “Algebraic generation of single domain computational grid for twin screw machines Part II – Validation”, *Advances in Engineering Software*, vol. 109, pp. 31–43, 2017.

[14] A. Kovacevic, “Three-Dimensional Numerical Analysis for Flow Prediction in Positive Displacement Screw Machines”, PhD thesis, City University London, 2002.

[15] *SCORG Help Manual v5.9*, Surrey, CR3 0BL: PDM Analysis Ltd, 2021.

[16] Z. Virag, M. Šavar, and I. Džijan, *Mehanika fluida II predavanja*, Zagreb: ITG d.o.o., 2017.

[17] E. M. Smirnov, A. G. Abramov, N. G. Ivanov, P. E. Smirnov, and S. A. Yakubov, “DNS and Rans/les-computations of complex geometry flows using a parallel multiblock finite-volume code”, *Parallel Computational Fluid Dynamics 2003*, pp. 219–226, 2004.

[18] S. Deck, F. Gand, V. Brunet, and S. Ben Khelil, “High-fidelity simulations of Unsteady Civil Aircraft Aerodynamics: Stakes and perspectives. application of zonal detached eddy simulation”, *Philosophical Transactions of the Royal Society A: Mathematical, Physical and Engineering Sciences*, vol. 372, no. 2022, p. 20130325, 2014.

[19] A. M. Joshi, D. I. Blekhman, J. D. Felske, J. A. Lordi, and J. C. Mollendorf, “Clearance analysis and leakage flow CFD model of a two-lobe multi-recompression heater”, *International Journal of Rotating Machinery*, vol. 2006, pp. 1–10, 2006.

[20] S. Sun, G. Singh, A. Kovacevic, and C. Bruecker, “Experimental and numerical investigation of tip leakage flows in a Roots blower”, *Designs*, vol. 4, no. 1, p. 3, 2020.

[21] “Ansys Fluent 12.0 Theory Guide - 4.5.2 Shear-Stress Transport (SST) k - ω Model”, *Ansys* [Online]. Available: www.afs.enea.it/project/neptunius/docs/fluent/html/ th/node67.htm. [Accessed: 27-Apr.-2022].

[22] “All there is to know about different mesh types in CFD”, *Manchestercfd* [Online]. Available: www.manchestercfd.co.uk/post/all-there-is-to-know-about-different-mesh-types-in-cfd. [Accessed: 18-Apr.-2022].

[23] P. R. Eiseman, “Grid Generation for Fluid Mechanics Computations”, *Annual Review of Fluid Mechanics*, vol. 17, pp. 487-522, 1985.

[24] *ANSYS Fluent User’s Guide-Release 15.0*, Canonsburg, PA 15317: Ansys Inc, 2013.

[25] L. He and M. L. Oldfield, “Unsteady Conjugate Heat Transfer Modeling”, *Journal of Turbomachinery*, vol. 133, no. 3, 2010.

[26] N. Basha, “Numerical analysis of oil injection in twin-screw compressors”, PhD thesis, City University London, 2021.

[27] N. Basha, A. Kovacevic, and S. Rane, “User defined nodal displacement of numerical mesh for analysis of screw machines in fluent”, *IOP Conference Series: Materials Science and Engineering*, vol. 604, no. 1, p. 012012, 2019.

[28] B. Patel, A. Kovačević, T. Plantegenet, T. Tam, “High speed particle image velocimetry for leakage flow inside the oil-free positive displacement rotary machines”, Journal paper draft, City University London, 2021.

[29] S. Mcdougald, B. W. Imrie, and B. N. Cole, “An Investigation of the Volumetric. Efficiency of a Roots Blower”, *International Compressor Engineering Conference*, 1974.

ATTACHMENTS

I. CD-R disc